Dynamics of discrete light bullets in passively mode-locked semiconductor lasers

Bachelor thesis

submitted by
Thomas Seidel

Supervisor: *PD Dr. Svetlana Gurevich*
Co-Supervisor: *Prof. Dr. Uwe Thiele*

Westfälische Wilhelms-Universität Münster

Contents

List of Figures

1. Introduction

The aim of this thesis is to analyse the transverse dynamic of *discrete light bullets*. Light bullets are short pulses of light which are localised in transverse and propagation directions and thus, are also referred as *laser solitons* [Vla+97; EPL05; EL13; Jav17]. The term soliton is not solely reserved for opticals waves but rather generally describes a spatially localised wave package which maintains its shape while propagating at a constant velocity. Indeed, solitons were firstly discovered in water waves by John Scott Russell in 1834 but it took another 60 years for their mathematical description [DP06]. Water waves are so-called *conservative* solitons. However, most of the physical applications of solitons - including the light bullets discussed in this thesis - are realised with *dissipative* solitons (or *autosolitons*) [AA05]. This subgroup of solitons considers the effect of nonlinear gain and/or loss mechanisms and shows different dynamics as conservative solitons [GA12].

Optical solitons are of particular interest because short light pulses are already used today to transfer information through optical fibers. But because of dispersion the signal quality decreases over longer distances. Hence, light pulses with improved stability properties are searched [SS13].

Recently, a regime of temporal localisation was predicted and experimentally demonstrated in a semiconductor laser with passive mode-locking [Mar+14]. These lasers use a semiconductor gain media which is brought into an excited state using an electrical current as a pump. However, also optically pumped semiconductor lasers exist. Passive mode-locking is widely used method to create short optical pulses [Hau00]. Additionally to the obligatory gain element a nonlinear loss element is added which is usually realised through a saturable absorber in the resonator. Saturable absorption is a property of a material which states that the absorption of a material decreases with increasing light intensity. In this long-cavity regime, the round trip-time τ is made much longer than the semiconductor gain recovery time $\tau_g \approx 1\,\mathrm{ns}$, which is the slowest variable in the system [GJ17].

By combining many lasers into an array one can achieve a much larger output and improve the characteristics of the output signal substantially by synchronising the frequencies of the individual lasers [BS08]. Conclusively, such lasers are used widely to generate short optical pulses with high repetition rates and optical frequency combs suitable for numerous applications [Del+06].

The model used in this thesis is based on the work of [GJ17]. However, instead of regarding a continuous system as it is done in the mentioned paper, we consider a discretised system in order to realise circular laser array with n lasers for n discretisation points. For the continuous case the transverse dynamic of a light bullet can be described by a partial differential equation which can be simplified by the discretisation to n complex coupled first order ordinary differential equations (see section 2).

Thus, in this thesis, we examine if discrete localised solitons (DLSs) exist in the given system and under which circumstances stable solutions can be achieved. Therefore, a bifurcation analysis in different system parameters is conducted.

The thesis is structured as follows. First, the considered model is presented and explained. Next, from appropriate approximations the regarded system of differential equations is deduced. Before starting with the analysis some important theoretical preliminaries are made which are supposed to clarify the mathematical context of the work. The first step in the analysis is done with a direct numerical time simulation in order to find stable DLSs which are then comprehensively examined. With the found stable fixed points a numerical continuation can be initialised to investigate the dynamics of the system to changes in different parameters, namely the gain value G_0, the line width enhancement factor α and the coupling c. The according results are presented in form of bifurcation diagrams. The stability along the branches and the present lasermodes are examined with a linear stability analysis.

2. Model

A passively mode-locked laser can be described by the generic Haus partial differential equation [Hau00]. This is a situation in which a broad-area gain chip is coupled to distant saturable absorber with teleoptics in self-imaging condition, as in [Gen+18]. Also the diffraction is supposed to be small such that as in [Bra+97] paraxial approximation can be used. [GJ17] concludes the following differential equation for the field profile $E(r_\perp, z, \sigma)$ over the slow time scale σ:

$$\begin{aligned}\partial_\sigma E = &\left(\sqrt{\kappa}\left[1 + \frac{1-i\alpha}{2}G(r_\perp, z, \sigma) - \frac{1-i\beta}{2}Q(r_\perp, z, \sigma)\right]\right. \\ &\left. - 1 + \frac{1}{2\gamma^2}\partial_z^2 + (d+i)\Delta_\perp\right)E(r_\perp, z, \sigma)\end{aligned} \tag{1}$$

where G is the gain, Q is the absorption, γ is the bandwith of the spectral filter, $\Delta_\perp = \partial_x^2 + \partial_y^2$ is the transverse Laplacian, κ is the power fraction of the power remaining in the cavity after each round trip, and α and β are the linewidth enhancements factors of the gain and absorber section, respectively. The carrier dynamics reads

$$\partial_z G = \Gamma G_0 - G(\Gamma + |E|^2) + \mathcal{D}_g \Delta_\perp G \tag{2}$$

$$\partial_z Q = Q_0 - Q(1 + s|E|^2) + \mathcal{D}_q \Delta_\perp Q \tag{3}$$

where G_0 is the pumping rate, $\Gamma = \tau_g^{-1}$ is the gain recovery rate, Q_0 is the value of the unsaturated losses, s is the ratio of the saturation energy of the gain and the saturable absorber sections and $\mathcal{D}_{g,q}$ are the scaled diffusion coefficients. Equation (1) indeed describes the whole dynamics of the system, however, it is very complex to solve because it consists of different dynamics: the dynamics of the two dimensional transverse profile, the dynamics in propagation direction and the evolution in time. Therefore it is an expedient approach to separate the transverse and longitudinal field:

$$E(r_\perp, z, \sigma) = A(r_\perp, \sigma)p(z). \tag{4}$$

where $p(z)$ is a short normalised temporal pulse of length τ_p and $A(r_\perp, \sigma)$ is a slowly evolving amplitude. Furthermore, the transverse field is rotationally symmetric and thus, can be analysed in only one dimension instead of two. Further approximations (for details see [GJ17]) simplify eq. (1) to following expression for the transverse field:

$$\partial_t A = (d + i)\Delta_\perp A + F(|A^2|) \cdot A. \tag{5}$$

The nonlinear function F of the intensity $P = |A|^2$ is given by

$$F(P) = \sqrt{\kappa}\left[1 + \frac{1 - i\alpha}{2} G_0 h(P) - \frac{1 - i\beta}{2} Q_0 h(sP)\right] - 1 \tag{6}$$

where G_0 is the pumping rate, Q_0 is the value of the unsaturated losses, s is the ratio of the saturation energy of the gain and the saturable absorber sections and $h(P) = (1 - e^{-P})/P$ [GJ17]. Interestingly, eq. (5) is, which governs the dynamics of the transverse profile, is a so called *Rosanov equation* that is known in the context of static transverse autosolitons in a bistable interferometer [GJ17].

For this thesis, the one dimensional case of eq. (5) needs to be discretised (or rather the transverse Laplacian). For any function $f(x)$ this can be achieved by considering the derivative as a difference quotient:

$$\partial_x^2 f(x) = \partial_x \left(\frac{f(x + h/2) - f(x - h/2)}{h}\right) \tag{7}$$

$$= \frac{f(x + h) - 2 \cdot f(x) - f(x - h)}{h^2}. \tag{8}$$

Now, $f(x + h)$ can be understood as the next, $f(x)$ as the current and $f(x - h)$ as the previous discretisation point. Conclusively, for n discretisation points we are dealing with n complex coupled first order ordinary differential equations:

$$\partial_t A_j = (d + i) \cdot c \cdot (A_{j+1} - 2A_j + A_{j-1}) + F(|A_j|^2)A_j. \tag{9}$$

The strength of the coupling is determined by the newly introduced parameter c. According to eq. (8) for $c \to \infty$ the system is expected to behave as in the continuous case. Mostly, in this thesis the coupling is small in order to examine the discrete behaviour of the system. It is also important to mention that in order to fulfill the idea of a circular array as in fig. 1 periodic boundaries are needed,

which means that the nearest neighbours of laser no. n are no. $n-1$ and laser no. 1.

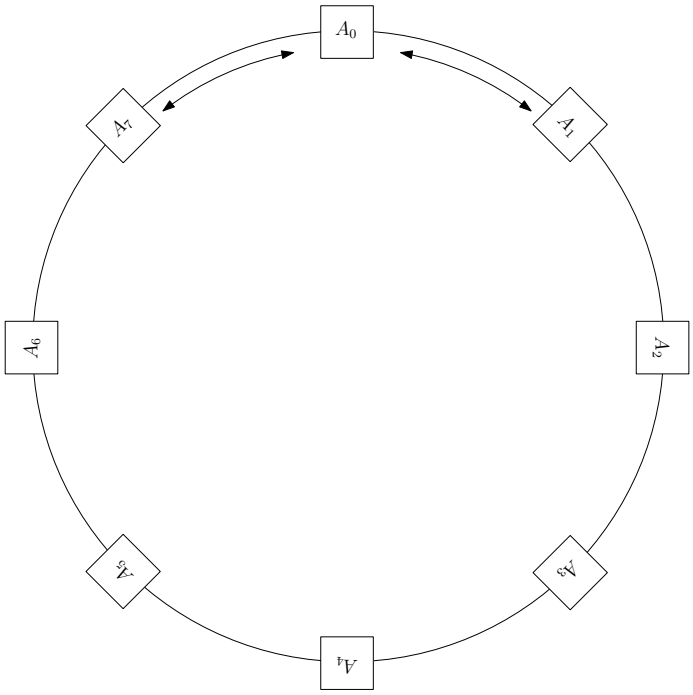

Figure 1: Schematic sketch of a circular laser array. The arrows indicate the coupling between the lasers. A_j denotes the transverse field of the respective laser.

3. Theoretical Preliminaries

Before the specific model is examined some important mathematical tools for the analysis of dynamical systems are introduced.

3.1. Nonlinear Systems

To begin with, we need to define what is meant by a *nonlinear system* by starting to define a *linear system*. A linear system is a system where the output is proportional to the input which can be expressed by the superposition principal for a linear function $f(x)$ with parameters $\alpha, \beta \in \mathbb{R}$ and $x, y \in \mathbb{R}^n$

$$f(\alpha x + \beta y) = \alpha f(x) + \beta f(y). \tag{10}$$

For a nonlinear system on the other hand this principle does not apply such that it is not easy to predict the output of the system to a change in input. Indeed, most systems in nature are nonlinear which explains why their study is of large interest [Str94].

The dynamics of a general state variable $x(t)$ can be described by differential equations which are continuous in time or discrete maps which are discrete in time. The analysed system is time-continuous such that we focus in differential equations of which three main groups exist: *ordinary*, *partial* and *delay* differential equations (ODE, PDE and DDE, respectively). In ODEs only derivatives of the unknown function with respect to one variable occur whereas for PDEs there are derivatives with respect to multiple variables. The highest occurring derivative defines the *order* of the differential equation. If $x(t)$ and its derivatives only appear with power one, the dynamical system is called *linear* and *nonlinear* otherwise. Generally, nonlinear systems are much more difficult to solve than linear ones and often the solution cannot be expressed in closed form. However, the dynamics of a nonlinear system can still be analysed by means of e.g., linear stability analysis and bifurcation theory.

3.2. Linear Stability Analysis

Points where the flux of a dynamical system becomes stationary in time are referred to as *fixed points*. So for the nonlinear system $\dot{\boldsymbol{x}} = f(\boldsymbol{x}, t)$ with the inner state $\boldsymbol{x}(t) = (x_1(t), ..., x_n(t)^T$ a fixed point $\boldsymbol{x}^*$ occurs when $f(\boldsymbol{x}^*, t) = 0$.

An important question when examining fixed points is to determine their stability as they can be *stable* or *unstable*. For this purpose the behavior of the system to small perturbations on fixed points is analysed [Str94]. For a stable fixed point the perturbation would slowly decrease and the system would return to the fixed point whereas for a unstable fixed point the perturbation would increase and the system would go over into a different state.

Thus, let us consider a small perturbation $\boldsymbol{x} = \boldsymbol{x}^* + \tilde{\boldsymbol{x}}$ with $|\tilde{\boldsymbol{x}}| \ll 1$ to the fixed point $\boldsymbol{x}^*$ in the dynamical system $\dot{\boldsymbol{x}} = f(\boldsymbol{x}, t)$. Then

$$\begin{aligned} \dot{\boldsymbol{x}} &= \dot{\boldsymbol{x}}^* + \dot{\tilde{\boldsymbol{x}}} = \dot{\tilde{\boldsymbol{x}}} && (11)\\ &= f(\boldsymbol{x}^* + \tilde{\boldsymbol{x}}, t) && (12)\\ &= \underbrace{f(\boldsymbol{x}^*, t)}_{=0} + f'(\boldsymbol{x}^*, t)\tilde{\boldsymbol{x}} + \mathcal{O}(\tilde{\boldsymbol{x}}^2) && (13)\\ \Leftrightarrow\ \dot{\tilde{\boldsymbol{x}}} &= f'(\boldsymbol{x}^*, t)\tilde{\boldsymbol{x}}. && (14) \end{aligned}$$

The fact that the $\mathcal{O}(\tilde{\boldsymbol{x}}^2)$ are left out describes a *linearisation* around $\boldsymbol{x}^*$ and gives the *linear* stability analysis its name. In eq. (14) $f'(\boldsymbol{x}^*, t)$ is called the *Jacobian matrix* evaluated at the fixed point:

$$f'(\boldsymbol{x}^*, t) = J = \left(\frac{\partial f_i}{\partial x_i}\right)\Bigg|_{\boldsymbol{x}^*} \tag{15}$$

Now let $\tilde{\boldsymbol{x}} = \boldsymbol{\varphi} e^{\lambda_i t}$. Then we are left with the linear eigenvalue problem

$$\lambda_i \boldsymbol{\varphi} = J\boldsymbol{\varphi} \tag{16}$$

with eigenvalues λ_i and eigenfunctions $\boldsymbol{\varphi}$. In general the eigenvalues are complex numbers. As $\tilde{\boldsymbol{x}} \propto e^{\lambda_i t} = e^{\mathrm{Re}(\lambda_i)t} \cdot e^{i\mathrm{Im}(\lambda_i)t}$ the perturbation will disappear for $\mathrm{Re}(\lambda_i) < 0\ \forall i$, whereas the perturbation will grow if $\mathrm{Re}(\lambda_i) > 0$ for any i. Hence, if the real part of all eigenvalues of the Jacobian are negative, $\boldsymbol{x}^*$ is a stable fixed point. However, if at least one eigenvalue has a positive real part the fixed point is unstable. The case $\mathrm{Re}(\lambda) = 0$ denotes *neutral stability* which means that one can't derive any conclusions on the stability from the linear stability analysis alone.

3.3. Bifurcations

A bifurcation occurs when a small change to a system parameter (the control parameter) causes a qualitative change in the system's behaviour. The results of a bifurcation analysis can be summarised in a *bifurcation diagram* where the bifurcation parameter is plotted against the location of the fixed points. The resulting lines of fixed points are referred to as *branches*. At a bifurcation point the stability of a solution branch changes which means that the real part of an eigenvalue passes the imaginary axis. Furthermore, additional branches can evolve from a bifurcation point. The exact behaviour at a bifurcation point defines the type of bifurcation. Each type can be described with the help of the so called *normal form*. All systems exhibiting a certain type of bifurcation are locally (around the equilibrium) topologically equivalent to the normal form of the bifurcation [Str94]. In the following several bifurcation types that are important for this thesis are presented.

3.3.1. Saddle-node Bifurcation

In a *saddle-node bifurcation* (or *fold bifurcation*) two fixed points arise from the bifurcation point, one of them being stable, the other one is unstable. The normal form of a saddle-node bifurcation is given by

$$\dot{x} = x^2 + r, \tag{17}$$

where r is a control parameter. Depending on the value of r three cases occur, which are visualised in the phase diagrams in fig. 2.

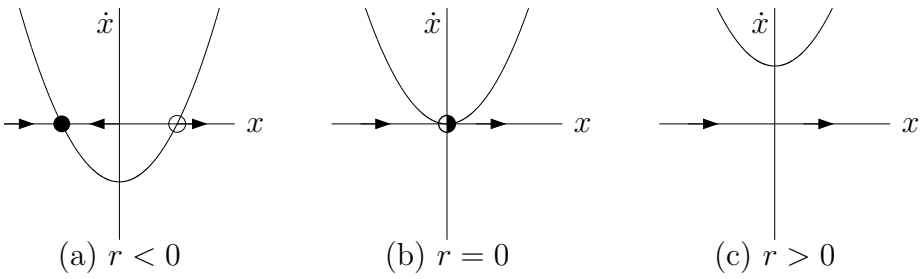

(a) $r < 0$ (b) $r = 0$ (c) $r > 0$

Figure 2: Phase diagram of eq. (17) for different values of the control parameter r. The circles highlight fixed points. A filled circle stands for a stable, an empty one for an unstable and a half filled for a metastable fixed point. The arrows indicate the direction of the velocity field.

For $r < 0$ two fixed points exist at $x^* = \pm\sqrt{|r|}$. To find their stability the respective Jacobian is regarded which simply is the derivative in this case because eq. (17) is one dimensional:

$$J = 2 \cdot x^*. \tag{18}$$

One finds that the fixed point at $x = -\sqrt{|r|}$ is stable while $x = \sqrt{|r|}$ is unstable. This can also be explained descriptively with the phase diagram (see fig. 2). Around the unstable fixed point the velocities point away from the fixed point meaning that a small perturbation would grow over time and thus the system changes its state. On the other hand, for the stable fixed point, the velocities point back towards the equilibrium such that a small perturbation would immediately be equalised by this reversing force.

When r is increased the fixed points move towards each other and eventually for $r = 0$ they annihilate. The resulting fixed point is metastable which means that it is stable against a small perturbation but unstable for larger ones. For $r > 0$ no fixed points exist. The results are summarised in the bifurcation diagram in fig. 3.

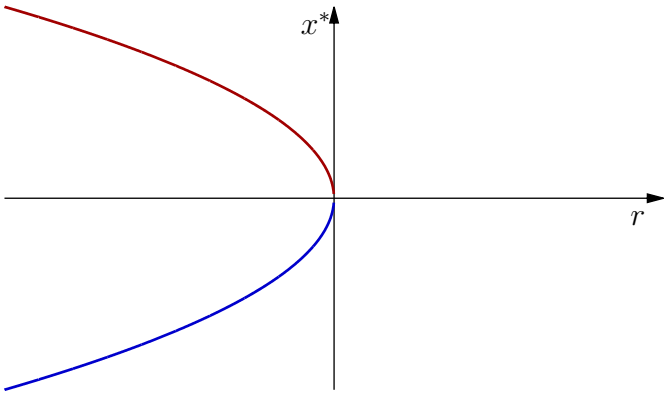

Figure 3: Bifurcation diagram of a saddle-node bifurcation. For $r < 0$ two fixed points at $\pm\sqrt{|r|}$ exist. The blue line denotes the stable and the red line the unstable fixed point.

3.3.2. Transcritical Bifurcation

The normal form of a *transcritical bifurcation* is given by

$$\dot{x} = r \cdot x - x^2 = x \cdot (r - x), \tag{19}$$

where r is a control parameter. Fig (4) shows the according phase diagram.

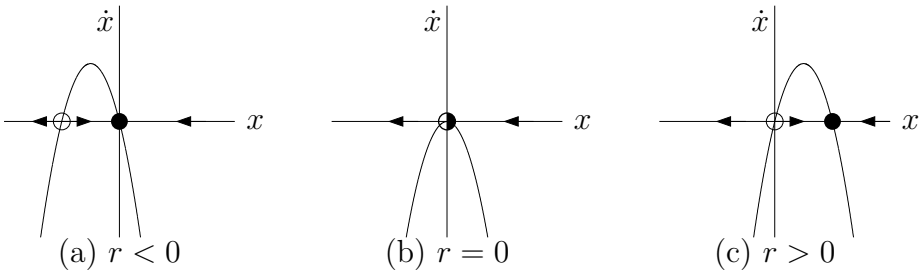

Figure 4: Phase diagram of eq. (19) for different values of the control parameter r. The circles denote a fixed point. A filled circle stands for a stable, an empty one for an unstable and a half filled for a metastable fixed point. The arrows indicate the direction of the velocity field.

Thus, the fixed points are located at $x^* = 0$ and $x^* = r$. The Jacobian is

$$J = r - 2 \cdot x^*. \tag{20}$$

For $r < 0$ the fixed point $x^* = 0$ is stable as the Jacobian is equal to r and therefore negative. $x^* = r$ on the other hand is unstable. For $r = 0$ the Jacobian is zero for $x^* = 0$ which means that it is a metastable fixed point. When r is increased to positive values the stability changes compared to negative values of r. The fixed point $x^* = 0$ is unstable while $x^* = r$ is stable. The according bifurcation diagram is shown in fig. 5.

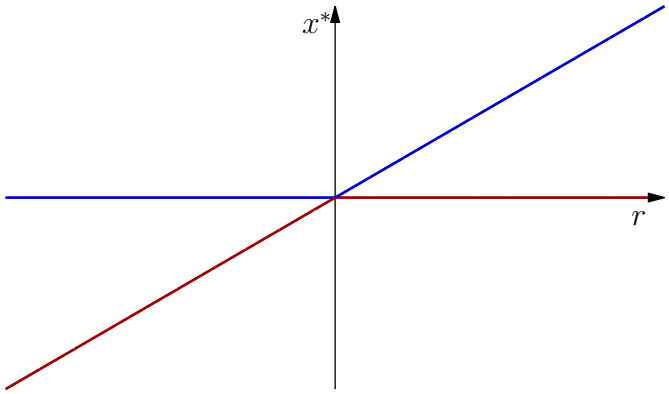

Figure 5: Bifurcation diagram of a transcritical bifurcation. For all $r \neq 0$ there are two fixed points. Their stability is swapped in the bifurcation point at $r = 0$. The blue/red line denotes the stable/unstable fixed point.

3.3.3. Hopf Bifurcation

The previously presented bifurcation types were discussed for one-dimensional dynamical systems but they have equivalent counterparts in multidimensional systems. The *Hopf bifurcation* (or *Andronov-Hopf bifrucation*) on the other hand can only occur in at least two dimensional systems. If a fixed point in a two-dimensional system is stable its eigenvalues must both have a negative real part. This can be expressed more precisely as the eigenvalues satisfy a quadratic equation with real coefficients: either the eigenvalues are both real and negative or they are complex conjugates [Str94]. In the first case they will cross the imaginary axis one after the other and describe one of the previously discussed bifurcation types. In the second case of complex conjugate eigenvalues, they will cross the imaginary axis simultaneously. This process is characteristic for a Hopf bifurcation.

Two types of Hopf bifurcations are differentiated: *supercritical* and *subcritical*. First, let us regard a system which reaches its equilibrium through a damped oscillation and the damping rate depends on a parameter r which can turn the decay into a growth for some critical value r_c (see fig. 6). Then at $r = r_c$ a supercritical Hopf bifurcation occurs.

The following system provides a simple example of a supercritical Hopf bifurcation in polar coordinates:

$$\dot{\rho} = r\rho - \rho^3, \tag{21}$$

$$\dot{\varphi} = \omega + b\rho^2, \tag{22}$$

where the parameter r controls the stability of the fixed point $\rho^* = 0$, ω defines the frequency of infinitesimal oscillations and b describes the dependence of the frequency on the amplitude. Rewriting the system in Cartesian coordinates simplifies to find the eigenvalues:

$$\dot{x} = rx - \omega y + \mathcal{O}(x^2, y^2) \tag{23}$$

$$\dot{y} = \omega x + ry + \mathcal{O}(x^2, y^2) \tag{24}$$

Now, one sees that in the origin the Jacobian matrix

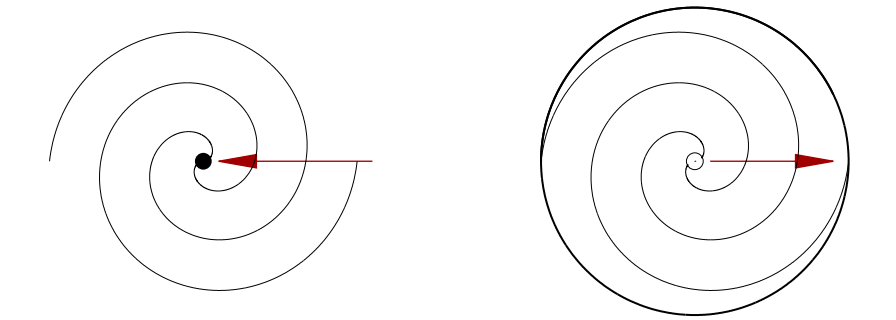

(a) $r < r_c$ (b) $r > r_c$

Figure 6: Phase diagram of a supercritical Hopf bifurcation for r below and above the critical value r_c (upper) and schematic sketch of the time evolution of the oscillation dynamics (lower). In (a) the oscillation is damped such that the system is attracted (indicated by the red arrow) to the stable equilibrium in the centre (filled circle). In (b) the amplitude of the oscillation increases which means that the origin in the phase diagram and the according spiral becomes unstable (empty circle) and drifts towards a so called *limit cycle* (thick line) [Str94].

$$J = \begin{pmatrix} r & -\omega \\ \omega & r \end{pmatrix} \tag{25}$$

has the complex conjugated eigenvalues $\lambda = r \pm i\omega$ and thus, the critical value for the system is $r = 0$.

An example for system showing a subcritical Hopf bifurcation is given similarly but this time the cubic term ρ^3 is destabilising:

$$\dot{\rho} = r\rho + \rho^3 - r^5, \tag{26}$$

$$\dot{\varphi} = \omega + b\rho^2. \tag{27}$$

This leads to new limit cycles in the phase diagram (see fig. 7).

To examine whether a Hopf bifurcation is sub- or supercritical can be decided with an analytical criterion (see [GH83]) but it is easier to use a compute simulation and check the limit cycles which appear around the Hopf bifurcation [Str94].

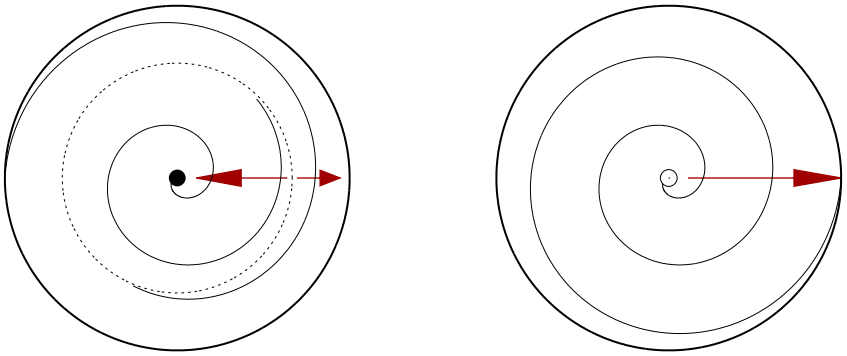

(a) $r < r_c$ (b) $r > r_c$

Figure 7: Phase diagram of a subcritical Hopf bifurcation with r below and above the critical value. In (a) one sees that there are two attractors, a stable limit cycle (thick line) and a stable fixed point in the origin (filled circle). In between an unstable limit cylcle is located (dashed line). The red arrows indicate the respective attracting force. For increasing r the unstable limit cycle tightens like a noose around the stable fixed point until eventually for $r = r_c$ the amplitude of the unstable cycle is zero which leaves the originunstable. Now, the large-amplitude limit cycle is the only attractor [Str94].

3.4. Numerical Approximations to ODEs

As described in section 3.1, in some cases it is not possible to express a solution of a nonlinear dynamical system in closed analytical form. However, there are numerical methods to approximate the solution. The analysed system is based on a *initial value problem* and thus, we want to focus on numerical solutions of this kind of differential equations. An initial value problem is a first order ODE such as

$$\dot{x} = f(x(t), t) \tag{28}$$

with an initial condition $x_0 = x(t_0)$. Indeed, any dynamical system of the order n can be rewritten into n equations of first order. The *Euler-method* uses the fact that for ordinary differential equations the derivation of any point is known. So if x_0 is a solution of eq. (28), its flux at this point is $\dot{x}_0 = f(x_0, t_0)$. Thus, during a small increment in time Δt the distance $f(x_0, t_0) \cdot \Delta t$ is covered assuming that the flux doesn't change during Δt. Of course this isn't the case but for a sufficiently small increment the error which is being made becomes negligible.

Hence the position $x(t_0 + \Delta t)$ is approximately $x_0 + f(x_0, t_0) \cdot \Delta t$. This system can be applied iteratively, such that

$$x_{n+1} = x(t_{n+1}) = x_n + f(x_n, t_n) \cdot \Delta t, \tag{29}$$

where $t_n = t_0 + n\Delta t$. Basically the Euler-method describes a Taylor expansion of first order in each point, meaning that the error made in each step, referred to as the *local truncation error*, is $\mathcal{O}(\Delta t^2)$. It can be shown that the *global truncation error* (the error between the exact solution $x(t_n)$ and the approximate solution x_n) is $\mathcal{O}(\Delta t)$ [Str94]. Therefore the Euler-method is first order. Naively one could say that in order to increase the accuracy of the numerical method you should just decrease Δt. However, this makes the whole procedure very computationally intense which one tries to avoid.

Thus, methods of higher orders are needed. This can be achieved e.g., by appropriately combining the derivatives at several different points over the time step interval. These approach is realised by the *family of Runge-Kutta methods*. In particular, for the *forth order Runge-Kutta method* (see fig. 8) the next step from a given solution x_n is

$$x_{n+1} = x_n + \frac{1}{6}(k_1 + 2k_2 + 2k_3 + k_4)\Delta t \tag{30}$$

with

$$k_1 = f(x_n, t_n), \tag{31}$$

$$k_2 = f(x_n + \frac{1}{2}k_1\Delta t, t_n + \frac{1}{2}\Delta t), \tag{32}$$

$$k_3 = f(x_n + \frac{1}{2}k_2\Delta t, t_n + \frac{1}{2}\Delta t), \tag{33}$$

$$k_4 = f(x_n + k_3\Delta t, t_n + \Delta t). \tag{34}$$

Here the local truncation error is $\mathcal{O}(\Delta t^5)$ while the global truncation error is $\mathcal{O}(\Delta t^4)$ [Gur]. This means that when e.g. a step size of $h/2$ is used the global truncation error is $(1/2)^4 = 1/16$ of the error made for a step size h.

One could conclude that using Runge-Kutta methods of higher orders improves the accuracy for a given step size. However, this only applies up to some limit given by the so-called *Butcher barrier*. It states that the amount of stages m grows

faster than the order p. Or in other words, for $m \geq 5$ there are no Runge-Kutta methods with the convergence order $p = m$ [Gur]. Indeed, to reach order five $m = 6$ is required. Thus, the forth-order Runge-Kutta method is generally regarded as the best trade-off between a fast computation speed and a low error [Str94].

One possible way to improve the accuracy of the Runge-Kutta method is to implement an adaptive step-size control which makes it possible to scan areas with little change with a larger stepsize and thus, reduce the overall runtime without compromising on accuracy.

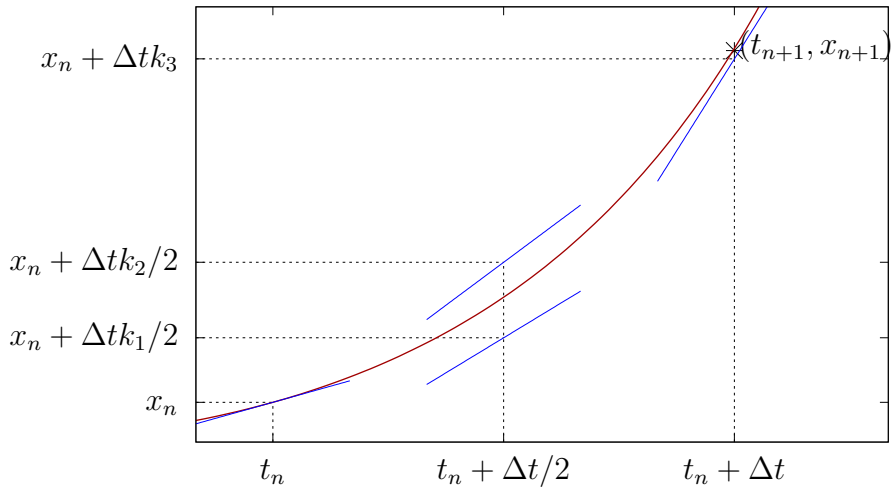

Figure 8: Visualisation of the fourth-order Runge-Kutta method. The red line describes the course of $x(t)$, the blue lines are the slopes k_i.

3.5. Numerical Continuation

The *numerical continuation* is a very useful tool in the analysis of dynamical systems because it allows one to examine the behaviour in the parameter space and hence, to follow the stable and unstable solution branches. Furthermore, bifurcations can be detected which offers the possibility to find new solution branches. Finally, bifurcation points can be tracked in higher dimensional parameter spaces (e.g. *two-parameter-continuation*). For this thesis the software package `AUTO-07P` is used [Doe+07]. In the following the necessary steps to follow a branch in the parameter space are presented.

Let $\dot{\boldsymbol{x}} = \boldsymbol{f}(\boldsymbol{x}, \mu)$ be a system of n ordinary differential equations with one free parameter μ and $\boldsymbol{x}_0^* = (x_{0,1}^*, x_{0,2}^*, ..., x_{0,n}^*)$ is a solution for $\mu = \mu_0$. The solution

$\boldsymbol{x}_0^*$ is called an *initial guess* and can be obtained e.g., from direct numerical simulations. Now we want to compute the solution $\boldsymbol{x}_1^*$ for the parameter $\mu_1 = \mu_0 + \Delta\mu$. Therefore, the tangent of the curve $\boldsymbol{x}^*(\mu)$ at $(\boldsymbol{x}_0^*, \mu_0)$ is used in order to make a first prediction $\boldsymbol{x}_1^{*(0)}$ at μ_1 [Thi17]:

$$\boldsymbol{x}_1^{*(0)} = \boldsymbol{x}_0^* + \Delta\mu \frac{\partial \boldsymbol{x}^*}{\partial \mu}\bigg|_{\boldsymbol{x}_0^*} \tag{35}$$

The slope can easily be computed when differentiating $\boldsymbol{f}(\boldsymbol{x}^*(\mu), \mu) = 0$:

$$\left[\underbrace{\frac{\partial \boldsymbol{f}}{\partial \boldsymbol{x}}}_{\text{Jacobian}} \frac{\partial \boldsymbol{x}}{\partial \mu} + \frac{\partial \boldsymbol{f}}{\partial \mu} \right]_{(\boldsymbol{x}_0^*, \mu_0)} = 0 \tag{36}$$

$$\Leftrightarrow \quad \frac{\partial \boldsymbol{x}}{\partial \mu}\bigg|_{(\boldsymbol{x}_0^*, \mu_0)} = -\left[\left(\frac{\partial \boldsymbol{f}}{\partial \boldsymbol{x}} \right)^{-1} \cdot \frac{\partial \boldsymbol{f}}{\partial \mu} \right] \bigg|_{(\boldsymbol{x}_0^*, \mu_0)} . \tag{37}$$

The approximation $\boldsymbol{x}_1^{*(0)}$ of the solution $\boldsymbol{x}_1^*$ is supposed to satisfy $\boldsymbol{f}(\boldsymbol{x}_1^{*(0)}, \mu_1) = 0$ but as only a linear approximation was used the error can expected to be significant. Thus, the next step is to "improve" the guess for $\boldsymbol{x}_1^*$. This can be achieved with the *Newton's method* which can compute roots of functions up to an arbitrary order. The iteration is given by

$$\boldsymbol{x}_1^{*(n+1)} = \boldsymbol{x}_1^{*(n)} - \left(\frac{\partial \boldsymbol{f}}{\partial \boldsymbol{x}} \right)^{-1} \bigg|_{(\boldsymbol{x}_1^{*(n)}, \mu_0)} \cdot \boldsymbol{f}\left(\boldsymbol{x}_1^{*(n)} \right). \tag{38}$$

Then one can return to change μ, find the root for the new parameter and hence, continue to follow the solutions branch.

This method is unproblematic until the branch approaches a fold at some $\mu = \mu_\mathrm{f}$, which indeed is a bifurcation type that occurs frequently.The problem is that for $\mu < \mu_\mathrm{f}$ two solutions exist while there is none for $\mu > \mu_\mathrm{f}$ [Thi17]. To follow the branch around the fold, a parameter which is unique along the branch is needed. The issue is addressed with the *Pseudo-arclength continuation* of which only the general idea is presented at this point. The control parameter μ is interpreted as an additional element of the extended solution $\boldsymbol{y^*} = (\boldsymbol{x}^*, \mu)$. Instead of μ the new control parameter is the arclength s, which can be approximated locally with Pythagoras' theorem:

$$|\boldsymbol{x}^*|^2 + (\Delta\mu)^2 = (\Delta s)^2. \tag{39}$$

This condition $\boldsymbol{p}(\boldsymbol{x}^*, \mu, s)$ supplements $\boldsymbol{f}(\boldsymbol{x}^*, \mu)$ such that we can introduce the extended system

$$\boldsymbol{E}(\boldsymbol{y}^\star, s) = \begin{pmatrix} \boldsymbol{f}(\boldsymbol{x}^*, \mu) \\ \boldsymbol{p}(\boldsymbol{x}^*, \mu, s) \end{pmatrix}. \tag{40}$$

The next steps are equivalent to the described method above. In order to compute the solution at $s_{j+1} = s_j + \Delta s$ a tangent of the curve $\boldsymbol{y}^\star(s)$ at $(\boldsymbol{y}_j^*, s_j)$ is used as a predictor for $\boldsymbol{y}_{j+1}^{*(0)}$. To find the root $\boldsymbol{y}_{j+1}^*$ up to the desired exactness Newton's method is applied [Thi17].

4. Analysis of the System

4.1. Existence of multistability

The first steps in the analysis of the system described by eq. (9) are conducted with a direct numerical time simulation. The implementation is realised in `Python` for $N = 51$ discretisation points. The initial state for the simulation consists of a (discretised) Gauß-peak with amplitude B and arbitrary width l for the real part of A_j:

$$A_{j,\text{initial}} = B \cdot \exp\left[-\left(\frac{j-(N-1)/2}{l}\right)^2\right]. \tag{41}$$

The system parameters are chosen in reference to [GJ17] such that one can expect that the system evolves towards a stable attractor of the dynamics in form of discrete localized states with different number of active lasers. In figs. 9a to 9d the initial states for two different with l are displayed together with the result of a direct numerical simulation, whereas fig. 9e shows $\int |A|^2$ in dependence on the width l of numerous initial states. Here, $\int |A|^2 := \sum_j |A_j|^2$ is the total intensity of all lasers.

It was found, that the system evolves to various attractors with different numbers of active lasers depending on the width l of the initial state. The various attractors can be seen in form of steps in fig. 9e. To which attractor the system evolves depends solely on the initial state (in this case represented by different widths l of the initial Gauß'ian peak). This phenomenon is referred to as *multistability*. The idea of multistabilities will occur repetitively throughout the thesis. In order to simplify the calculations mostly the minimal one laser solution (e.g. fig. 9b) and the three laser solution (e.g. fig. 9d) will be regarded. But it was also found that stable states with an even number of lasing lasers exist.

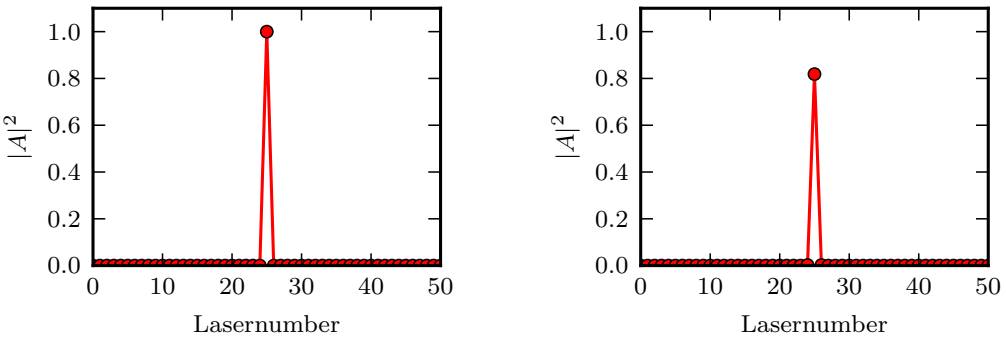

(a) $l = 0.1$ initial state

(b) $l = 0.1$ final state

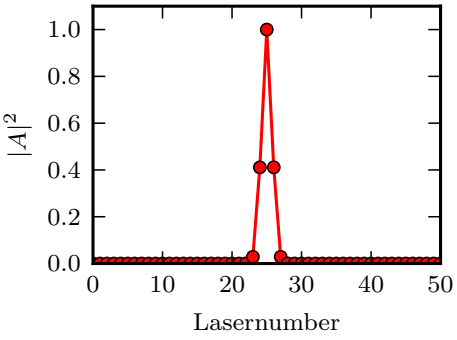

(c) $l = 1.5$ initial state

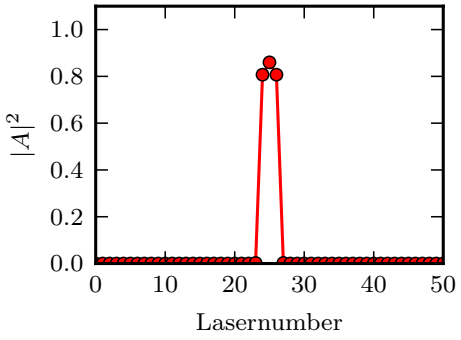

(d) $l = 1.5$ final state

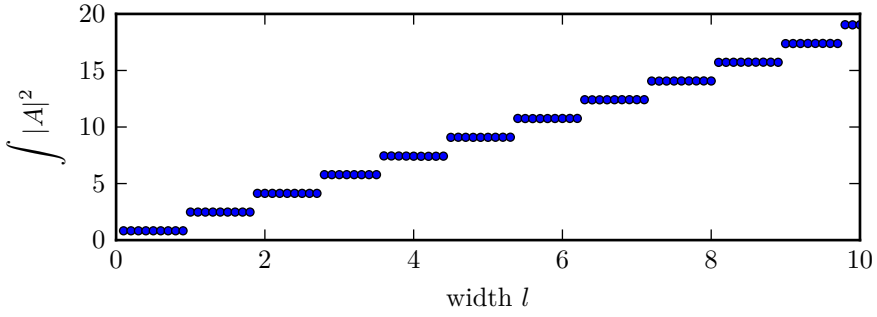

(e) Dependence of $\int |A|^2$ after a direct numeric simulation on the width l of a Gaußian initial state.

Figure 9: In figs. 9b and 9d the solutions after $t_{\text{end}} = 500$ time steps of the initial states in figs. 9a and 9c are displayed. This process is repeated iteratively for many different width, which results in fig. 9e. The used parameters are $(G_0, Q_0, \alpha, \beta, c, d, s, \kappa = 0.365, 0.3, 1.5, 0.5, 0.004, 0, 30, 0.8)$.

4.2. Carrier frequency of the solution

In section 4.1 it was found that stable DLSs with respect to $\int |A|^2$ exist. However, this only applies for the norm but not for $\mathrm{Re}(A)$ and $\mathrm{Im}(A)$, respectively. Both oscillate with a certain carrier frequency ω when the stable state is reached. Animations of the time evolution for two initial states can be found in appendix A. The oscillation of the real and imaginary part shows that the system possesses a phase shift symmetry. In order to break the symmetry and thus find fixed points for $\mathrm{Re}(A)$ and $\mathrm{Im}(A)$ we use the ansatz

$$A_j(t) = a_j e^{-i\omega t}, \tag{42}$$

where ω is a so-called frequency shift or a spectral parameter and a_j describes a time independent amplitude. This ansatz also explains why $|A_j|^2 = a_j e^{-i\omega t} \cdot \bar{a}_j e^{i\omega t} = |a_j|^2$ denotes a fixed point. Now eq. (42) can be substituted into eq. (9). When regarding a steady state ($\partial_t a_j = \partial_t \omega = 0$) this leads to a the following equation:

$$(d+i) \cdot c \cdot (a_{j+1} - 2a_j + a_{j-1}) + i\omega a_j + F(|a_j|^2)a_j = 0. \tag{43}$$

At this point it makes sense to separate the equation's real and imaginary part as it necessary for the implementation of the numerical continuation. Therefore, let $a_j = u_j + iv_j$ with $u_j, v_j \in \mathbb{R}$, then eq. (43) can be split into

$$d \cdot c\Delta u_j - c\Delta v_j - \omega v_j + F_r(|a_j|^2)u_j - F_i(|a_j|^2)v_j = 0, \tag{44}$$

$$d \cdot c\Delta v_j + c\Delta u_j + \omega u_j + F_i(|a_j|^2)u_j + F_r(|a_j|^2)v_j = 0, \tag{45}$$

where $\Delta u_j = u_{j+1} - 2u_j + u_{j-1}$, $\Delta v_j = v_{j+1} - 2v_j + v_{j-1}$ and

$$F_r(|a_j|^2) = \mathrm{Re}(F(|a_j|^2)) = \sqrt{\kappa}\left[1 + \frac{1}{2}G_0 h(P) - \frac{1}{2}Q_0 h(sp)\right] - 1, \tag{46}$$

$$F_i(|a_j|^2) = \mathrm{Im}(F(|a_j|^2)) = \sqrt{\kappa}\left[-\frac{\alpha}{2}G_0 h(P) + \frac{\beta}{2}Q_0 h(sp)\right]. \tag{47}$$

Now, from one of eqs. (44) and (45) the carrier frequency ω can be computed explicitly using the steady states found in direct numerical simulation at an arbitrary point in time as they determine both u_j and v_j.

$$\omega = -\frac{1}{u_j}(dc\Delta v_j + c\Delta u_j) - F_i(|a_j|^2) - \frac{v_j}{u_j}F_r(|a_j|^2) \tag{48}$$

In the animations in the supplementary material (see appendix A) also the phase φ_j for each laser is displayed. And as $\varphi_j = \arctan\left(\frac{v_j}{u_j}\right)$ the phase is time invariant as well for a steady state. Interestingly it was found, that for a steady state neighbouring lasers are out of phase even if they were initialised in phase (see `2-laser-phase-change.mp4` in appendix A).

4.3. Detailed description of the solution's slopes

As described above the minimal nontrivial localised solution for the system consists of one lasing laser which can be the central or any laser. In fig. 9b it appears that $|A|^2 = 0$ for all the other lasers but this can be described more precisely. Let the lasing laser be A_0 and with the assumption that $A_j \gg A_{j+1}\ \forall j \geq 0$ and $|A_j|^2 \approx 0\ \forall j \neq 0$ we find for $j = 1$ that

$$\underbrace{\dot{A}_1}_{\substack{=0\\ \text{(steady state)}}} = \underbrace{F(|A_1|^2)}_{\approx F(0)} A_1 + (d+i)\cdot c \cdot (\underbrace{A_2}_{\approx 0} - 2A_1 + A_0) \tag{49}$$

$$\Rightarrow\ A_1 \approx \frac{(d+i)c}{2(d+i)c - F(0)} A_0. \tag{50}$$

This method can be applied recursively such that

$$A_j \approx \left(\frac{(d+i)c}{2(d+i)c - F(0)}\right)^j A_0. \tag{51}$$

When plotting the steady state of the minimal solution on a logarithmic scale this assumption is confirmed (see fig. 10).

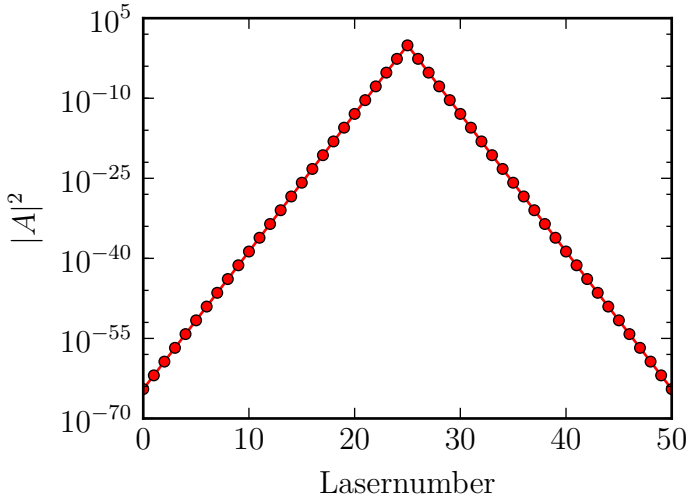

Figure 10: Steady state shown in fig. 9b on a logarithmic scale. One sees that the slopes towards the central laser are linear such that eq. (51) is validated.

4.4. The effect of different perturbations

In this section we consider a homogeneous steady state solution $A_j = 0 \ \forall j$ and add a small perturbation to this state. First of all, let the amplitude of the perturbation be constant such that $A_j = \varphi e^{\lambda t}$ with $\varphi \ll 1$. This expression can be plugged into eq. (9) which results in

$$\lambda A_j = F(|A_j|^2)A_j \quad \text{with } |A_j|^2 \approx 0 \tag{52}$$

$$\Leftrightarrow \ \mathrm{Re}(\lambda) = \mathrm{Re}(F(0)) = \sqrt{\kappa}\left[1 + \frac{G_0}{2} - \frac{Q_0}{2}\right] - 1. \tag{53}$$

This expression reveals the existence of a certain threshold gain G_{th} for which the homogeneous steady state becomes unstable. With eq. (53) the threshold gain value can be calculated:

$$\Rightarrow \ G_{\mathrm{th}} = \frac{2}{\sqrt{\kappa}} + Q_0 - 2. \tag{54}$$

For $Q_0 = 0.3, \kappa = 0.8$ the threshold gain is $G_{\mathrm{th}} = 0.536$. Two runs with $G_0 = 0.535$ and $G_0 = 0.537$ (see fig. 11) support the theory by showing the different

stabilities for $G_0 > G_{\text{th}}$ and $G_0 < G_{\text{th}}$, respectively.

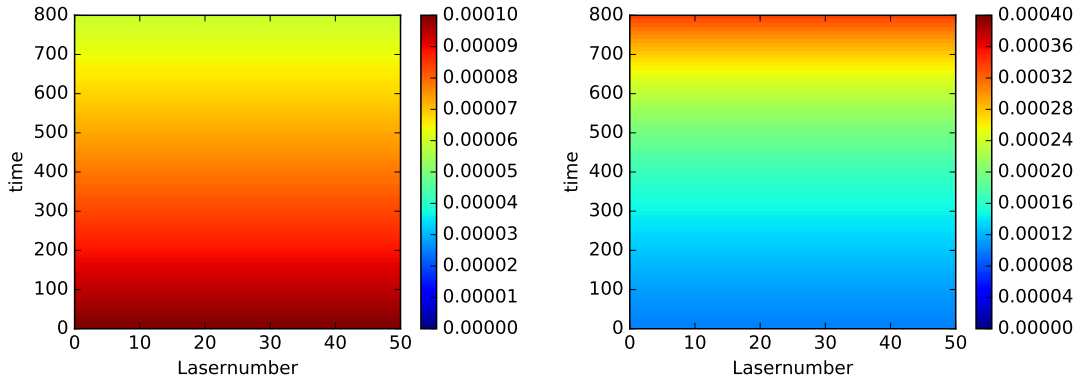

(a) $G_0 = 0.535$ (b) $G_0 = 0.537$

Figure 11: For $G_0 = 0.535$ the amplitude decreases which means it is a stable fixed point while for $G_0 = 0.537$ the amplitude increases which shows the instability of this fixed point. The amplitude of the perturbation is $\varphi = 0.01$ for both cases. Other parameters are $(\alpha, \beta, d, c) = (1.5, 0.5, 0.1, 0.004)$.

Indeed, the existence of a certain threshold gain value is expected as ordinary lasers, i.e. in laser pointers, rely on this principle. Above G_{th} the gain is larger than the loss in the resonator and the laser's output is dominated by stimulated emission. Thus, once kicked of (in this case by a small perturbation) the intensity increase rapidly.

Another interesting case considers a perturbation in the form of a plane wave, i.e., $A_j(t) = \varphi e^{iqj} e^{\lambda(q)t}$ with am small amplitude $\varphi \ll 1$ and a wave number q. When plugging this expression into the given differential equation one obtains

$$\lambda = F(0) + (d+i) \cdot c \cdot \left(e^{iq} - 2 + e^{-iq}\right) \tag{55}$$

$$= F(0) + 2(d+i) \cdot c \cdot (\cos(q) - 1) \tag{56}$$

$$\Rightarrow \ \text{Re}(\lambda) = \text{Re}(F(0)) + 2dc(\cos(q) - 1). \tag{57}$$

As $\cos(q) - 1 \leq 0$ the stability depends on $\text{Re}(F(0))$. Only if $\text{Re}(F(0)) > 0$ the system can get unstable for certain values of q (see fig. 13). This means that for values of G_0 around G_{th} stable states can still exist if initialised in the form of a plane wave with a certain wave number q. We examine this hypothesis via a direct numerical simulations for $q = 0$ (same as constant perturbation, see fig. 11b) and

$q = \pi$ (see fig. 12).

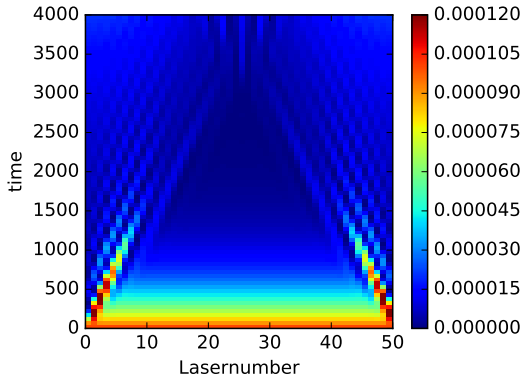

Figure 12: Initial state is a plane wave with $q = \pi$. The other parameters are the same as in fig. 11b. While for a constant perturbation the state becomes unstable, the plane wave is a stable.

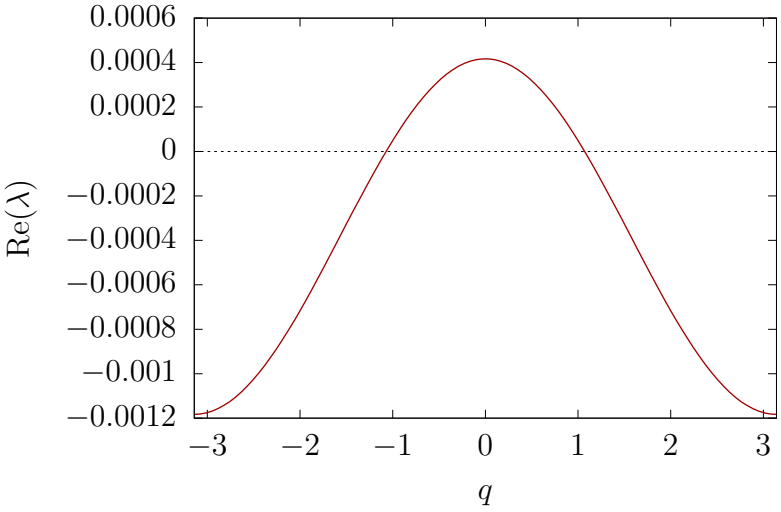

Figure 13: Visualisation of eq. (57) with parameters $(G_0, Q_0, \kappa, d, c) = (0.537, 0.3, 0.8, 0.01, 0, 004)$. For $\mathrm{Re}(\lambda) > 0$ the plane wave is expected to be unstable and for $\mathrm{Re}(\lambda) < 0$ to be stable. The maximum possible value for q is $\pm\pi$. It describes the case that the lasers are set to $\pm\varphi$ alternately.

4.5. Linear Stability Analysis of a localised solution

For the following analysis it is necessary to determine the stability of the system for different sets of parameters. We use the ansatz $A_j(t) = (a_j^* + \tilde{a}_j)e^{-i\omega t}$ to examine the reaction of the system to a small perturbation $\tilde{a}_j$ to a fixed point a_j^*. Substituting this expression into eq. (9) yields an differential equation for the perturbation:

$$\dot{\tilde{a}}_j = (d+i)\cdot c\cdot \Delta\tilde{a}_j + i\omega\tilde{a}_j + F(|a_j^*|^2)\tilde{a}_j + |a_j^*|^2\tilde{a}_j F'(|a_j^*|^2) + a_j^{*2}\bar{\tilde{a}}_j F'(|a_j^*|^2) \quad (58)$$

with $\Delta\tilde{a}_j = \tilde{a}_{j+1} - 2\tilde{a}_j + \tilde{a}_{j-1}$. As mentioned in section 4.2 we need to separate the real and imaginary parts: $\tilde{a}_j = \tilde{u}_j + i\tilde{v}_j, a_j^* = u_j^* + iv_j^*, F(|a_j|^2) = F_r + iF_i, F'(|a_j|^2) = F_r' + iF_i'$. Thus, the vector $\boldsymbol{a} = (\tilde{a}_1, \tilde{a}_2, ..., \tilde{a}_n)^T$ is replaced by $\boldsymbol{\psi} = (\tilde{u}_1, \tilde{v}_1, \tilde{u}_2, \tilde{v}_2, ..., \tilde{u}_n, \tilde{v}_n)^T$ and together with eq. (58) it leads to an eigenvalue problem:

$$\mathcal{L}(\boldsymbol{\psi}^*)\boldsymbol{\psi} = \lambda\boldsymbol{\psi} \quad (59)$$

with $\boldsymbol{\psi}^* = (u_1^*, v_1^*, ..., u_n^*, v_n^*)$. The linearisation operator $\mathcal{L}$ is a $2n \times 2n$-matrix (for n discretisation points) and has a linear part $\mathcal{M}$ and a nonlinear part $\mathcal{N}$,

$$\mathcal{M} = \begin{pmatrix} -2dc & 2c-\omega & dc & -c & 0 & 0 & 0 & \dots & dc & -c \\ -2c+\omega & -2dc & c & dc & 0 & 0 & 0 & \dots & c & dc \\ dc & -c & -2dc & 2c-\omega & dc & -c & 0 & \dots & 0 & 0 \\ c & dc & -2c+\omega & -2dc & c & dc & 0 & \dots & 0 & 0 \\ \vdots & \vdots & \vdots & \vdots & \vdots & \vdots & \ddots & \dots & \vdots & \vdots \\ c & dc & 0 & & \dots & & & & -2c+\omega & 2dc \end{pmatrix}$$

$$\mathcal{N}(\boldsymbol{\psi}^*) = \begin{pmatrix} F_r + 2u_1^*(u_1^*F_r' - v_1^*F_i') & -F_i + 2v_1^*(u_1^*F_r' - v_1^*F_i') & 0 & \dots \\ F_i + 2u_1^*(u_1^*F_i' + v_1^*F_r') & F_r + 2v_1^*(v_1^*F_r' + u_1^*F_i') & 0 & \dots \\ 0 & 0 & \ddots & \\ \vdots & \vdots & & \ddots \end{pmatrix}$$

The derivation of F is given by

$$F'(P) = \sqrt{\kappa}\left[\frac{1-i\alpha}{2}G_0 h'(P) - \frac{1-i\beta}{2}Q_0 h'(sP)\right] \tag{60}$$

$$\Rightarrow\ F'_r = \sqrt{\kappa}\left[\frac{1}{2}G_0 h'(P) - \frac{1}{2}Q_0 h'(sP)\right] \tag{61}$$

$$\Rightarrow\ F'_i = \sqrt{\kappa}\left[-\frac{\alpha}{2}G_0 h'(P) + \frac{\beta}{2}Q_0 h'(sP)\right] \tag{62}$$

with

$$h'(P) = \frac{e^{-P}(P+1)-1}{P^2} \tag{63}$$

$$h'(sP) = \frac{e^{-sP}(sP+1)-1}{sP^2}. \tag{64}$$

The eigenvalues λ and the respective eigenfunctions of $\mathcal{L}(\boldsymbol{\psi}^*) = \mathcal{M} + \mathcal{N}(\boldsymbol{\psi}^*)$ can be computed numerically using `Python` for any given DLS, either computed with a direct numerical simulation or via numerical continuation.

4.6. Continuation in G_0

So far, all calculations were conducted using direct numerical simulations. In this section first results of the numerical continuation are presented. As discussed before, eq. (9) possesses a phase shift symmetry. Thus, eqs. (44) and (45) are used for the implementation in `AUTO-07P` as otherwise the program would find an infinite number of solutions with the same intensity profile but different phases. In order to compute the solution for only one a_j an arbitrary phase must be chosen. Because all of the analysis are conducted with $N = 51$ discretisation points the phase of the central laser is defined to be zero: $v_{25} = 0$. As a starting point for the continuation the steady states found in direct numeric are used. But as they have a random phase they must be multiplied by $e^{-i\varphi_{25}}$ with φ_{25} being the phase of the central laser before they are inserted in `AUTO-07P`. This ensures $v_{25} = 0$.

The primary continuation parameter is the gain value G_0. The parameter is altered in order to examine for which values stable localised solitons can be found. A typical bifurcation diagram for DLSs with different numbers of lasing lasers and with $\int |A|^2$ as a norm is displayed in fig. 14. A corresponding bifurcation diagram

in (G_0, ω)-plane for the first two branches is shown in fig. 16.

In fig. 14 one can see that all branches bifurcate from G_{th} back in G_0. The according low power branches are unstable. Then, the branches undergo a fold bifurcation at F with additional Hopf bifurcations close by for higher numbers of lasing lasers. When analysing the number of Hopf bifurcations around F one finds that it is equal to the number of lasing lasers minus one. (Remark: for two lasers the main fold is almost at the same location as the Hopf bifurcation. This is why the marker looks like a black square rather than a green square and a black dot.) The high power branches remain stable up to the Hopf bifurcation H. Interestingly for the unstable area around F the four laser solution behaves differently from the other three branches. Instead of decreasing the intensity of all lasers, like the other branches do, the branch folds up to higher intensities. When looking at the profiles marked with the blue star (see fig. 15) one notices that they actually differ (even though their intensity profile is identical). A linear stability analysis reveals that one branch is stable while the other is unstable.

In the (G_0, ω)-plane one can see that the change along the stable branch of the carrier frequency is small. It increases slowly towards the main fold F and then grows approximately linearly with G_0. The carrier frequency is higher for the unstable low power branches because ω is inversely proportional to the intensity. On the whole branch the carrier frequency for the two laser soliton is higher than for the one laser soliton. This changes for $G_0/G_{\mathrm{th}} \to 1$ on the unstable branch when the two branches meet.

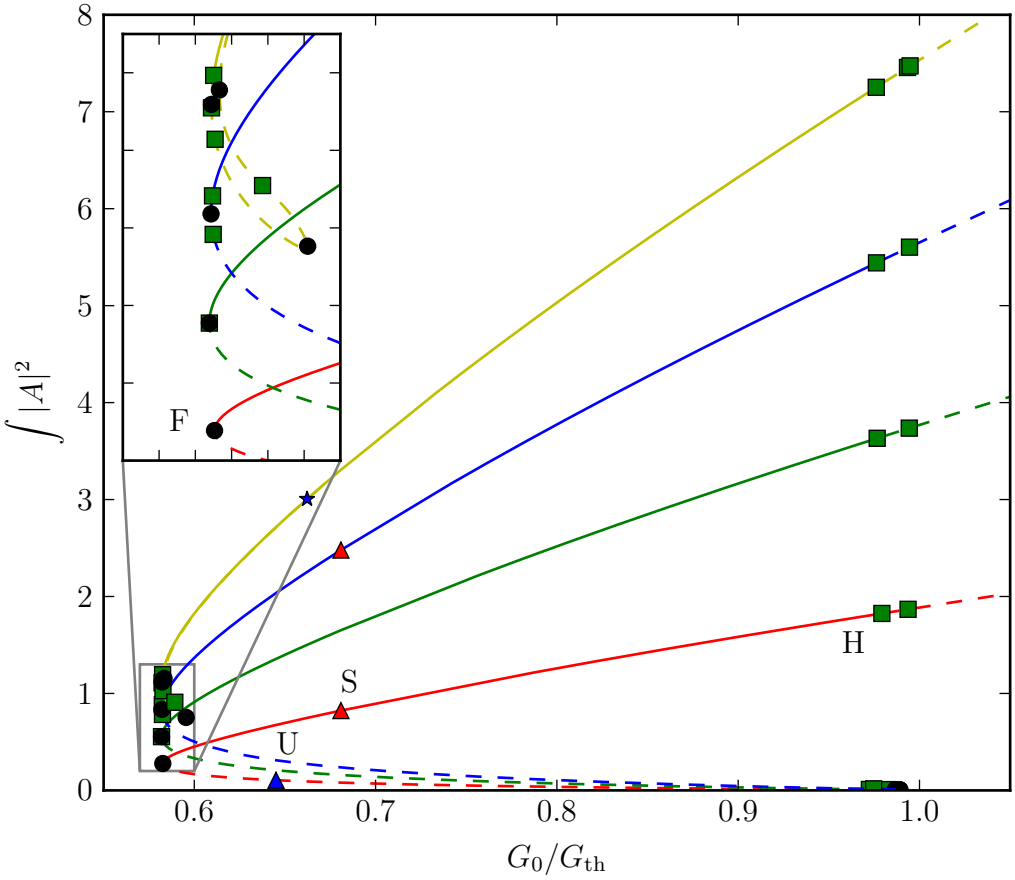

Figure 14: Bifurcation diagram for DLSs consisting of one (red), two (green), three (blue) and four (yellow) lasing lasers. The green squares denote Hopf bifurcations while the black dots stand for folds. The used parameters are the same as in fig. 9. The locations of the steady states shown in figs. 9b and 9d are marked with red triangles. The other labels are displayed for later references. Stable branches are marked with a solid line while unstable branches are dashed.

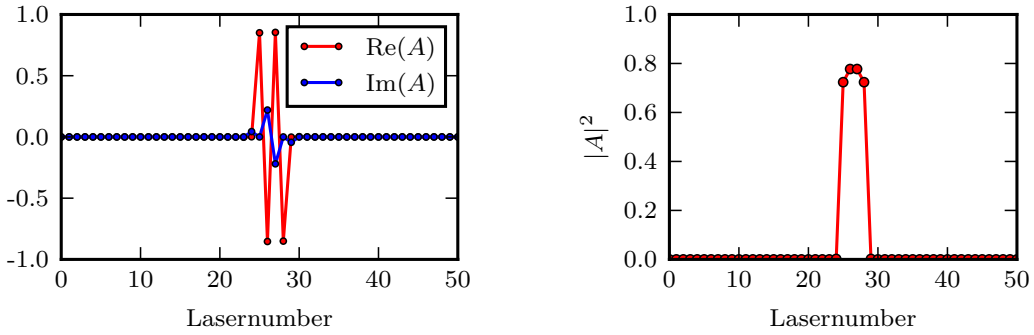

(a) solution profile on the stable branch

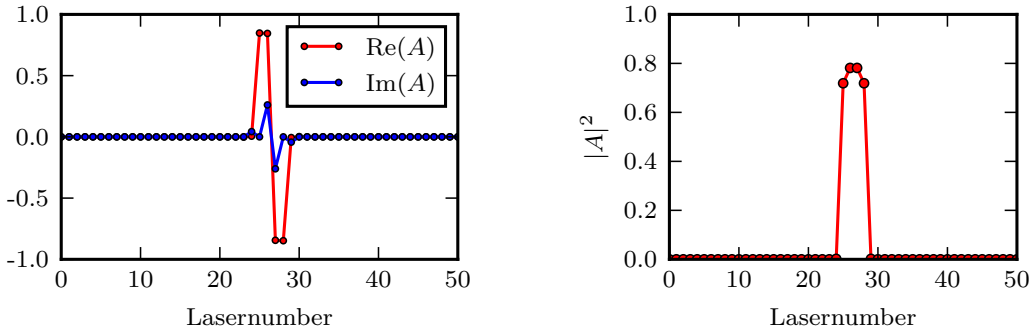

(b) solution profile on the unstable branch

Figure 15: Different solutions at the blue star marker in fig. 14 with the same intensity profile but different profiles for the real and imaginary parts. One of the DLSs is stable while the other is unstable.

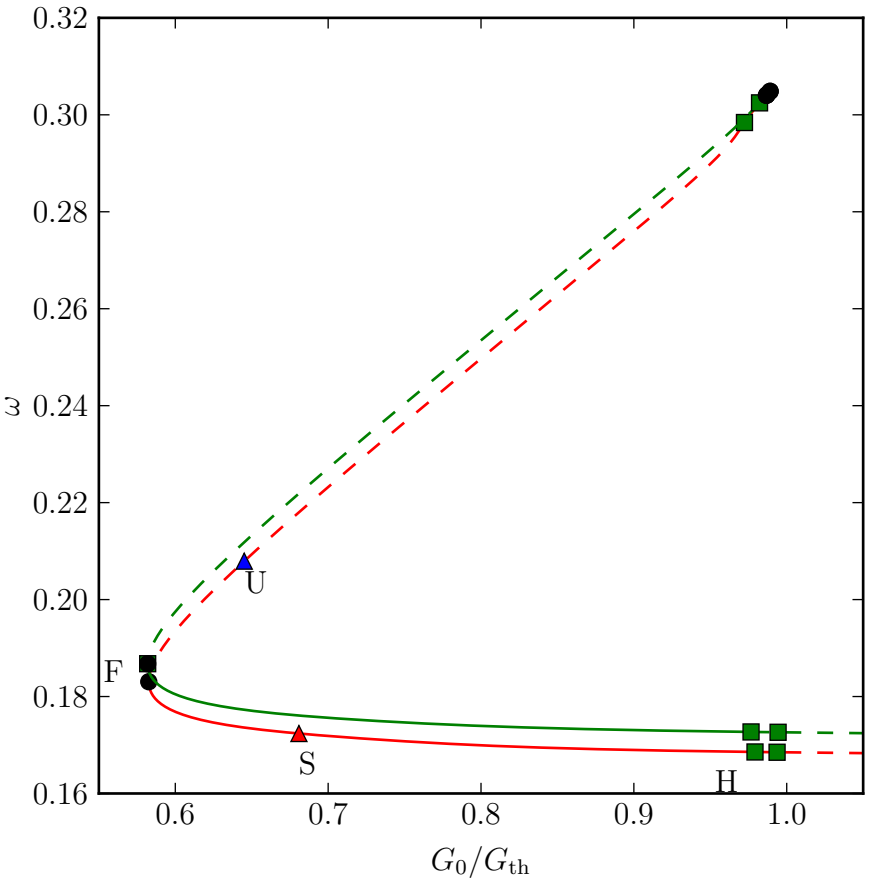

Figure 16: Bifurcation diagram for one (red) and two (green) laser soliton in the (G_0, ω)-plane. The markers and annotations define the same points as in fig. 14.

In fig. 14 it was mentioned that one part of each branch is stable while the rest is unstable. This can be validated when conducting a linear stability analysis. To simplify the analysis we begin with the minimal solution consisting of one lasing laser. The corresponding spectrum of leading critical eigenvalues for four different points along the branch is displayed in fig. 17.

In fig. 17a one can see an eigenvalue with a positive real part which means that the respective fixed point is unstable. At the fold F (see fig. 17b) the stability changes because the mentioned eigenvalue's real part is zero. Figure 17c displays the eigenvalues of the steady state in fig. 9b. The eigenvalue which changed its sign at the fold has now a negative real part. On the other hand the continuous spectrum of eigenvalues moves towards the right. On top of that four eigenvalues split of from the continuous spectrum. They denote a double Hopf bifurcation H as they change their signs at this point simultaneously (see fig. 17d). At $G_0 = G_{\mathrm{th}}$ the whole continuous spectrum of eigenvalues changes its sign making the resulting state highly unstable.

In fig. 14 additional Hopf bifurcations were found around the main fold for solutions with multiple lasing lasers. Accordingly in the respective eigenvalue spectrum (see fig. 18) pairs of eigenvalue cross the imaginary axis.

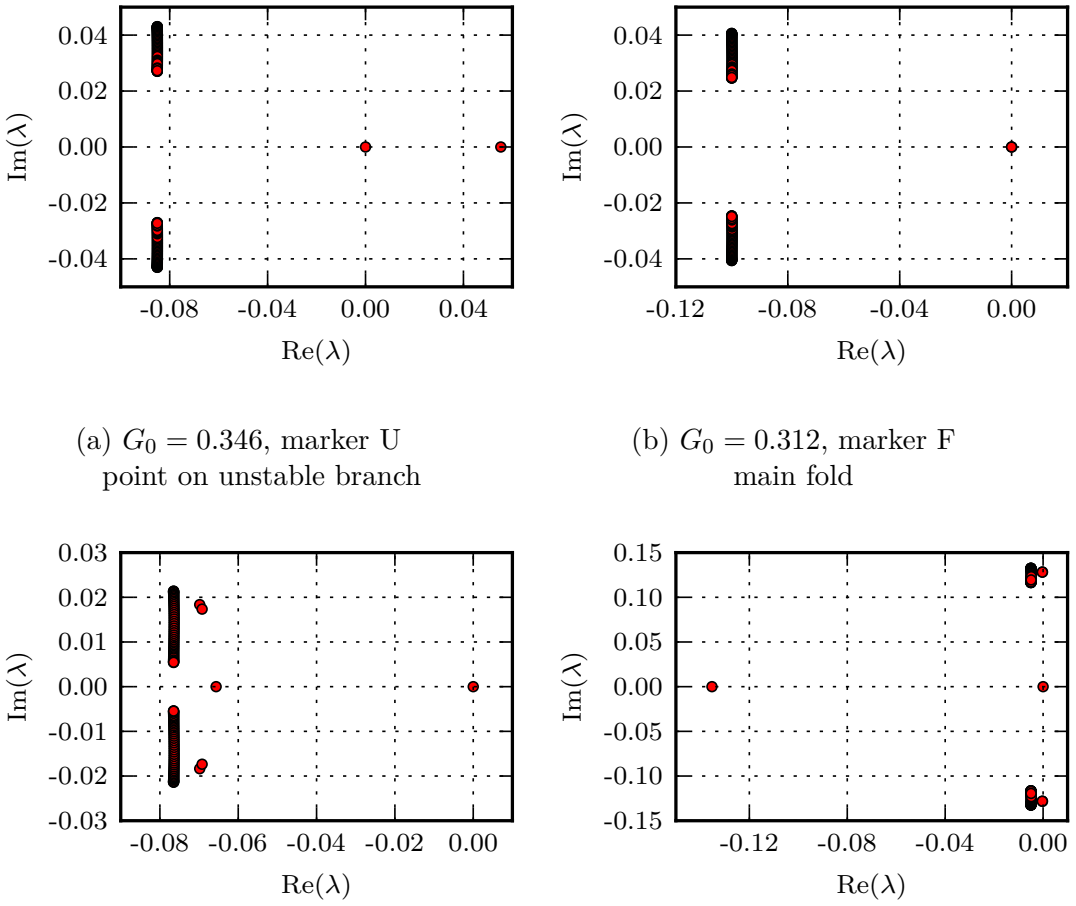

(a) $G_0 = 0.346$, marker U
point on unstable branch

(b) $G_0 = 0.312$, marker F
main fold

(c) $G_0 = 0.365$, marker S
point on stable branch

(d) $G_0 = 0.525$, marker H
Hopf bifurcation

Figure 17: Spectrum of eigenvalues for various points along the branch for one lasing laser. The mentioned markers refer to the annotations in fig. 14.

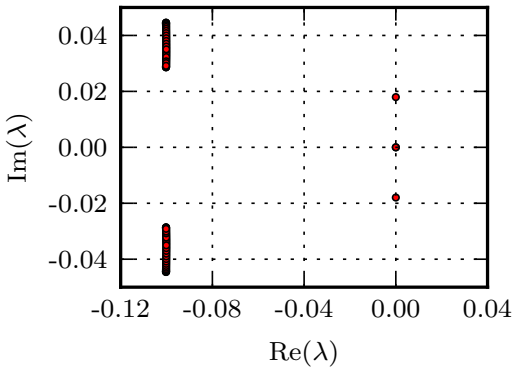

(a) two lasing laser DLS

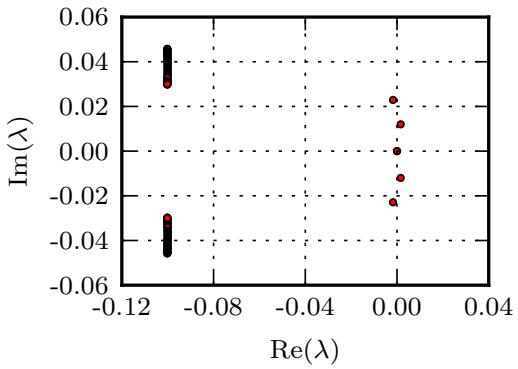

(b) three lasing laser DLS

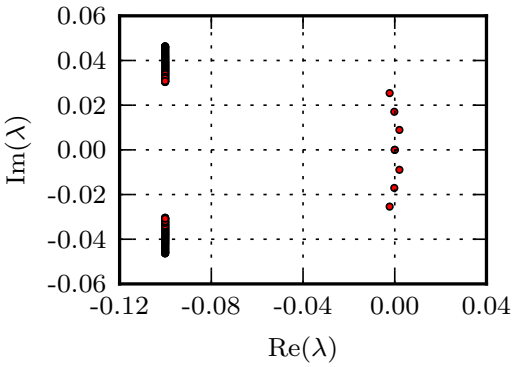

(c) four lasing laser DLS

Figure 18: Eigenvalue spectrum at the main fold for solutions with different numbers of lasing lasers (see fig. 14). The spectrum for the one laser soliton is in fig. 17b. For each additional lasing laser another pair of complex conjugated eigenvalues, which change their sign at around the main fold, occur. Each pair causes a Hopf bifurcation.

Besides all the eigenvalues which don't rest while moving along the branch there is the eigenvalue $\lambda = 0$ which is constant for all G_0 (see fig. 17). This is a so called *neutrally stable eigenvalue*. The according eigenvector as well as the real and imaginary part of the solution are displayed in fig. 19.

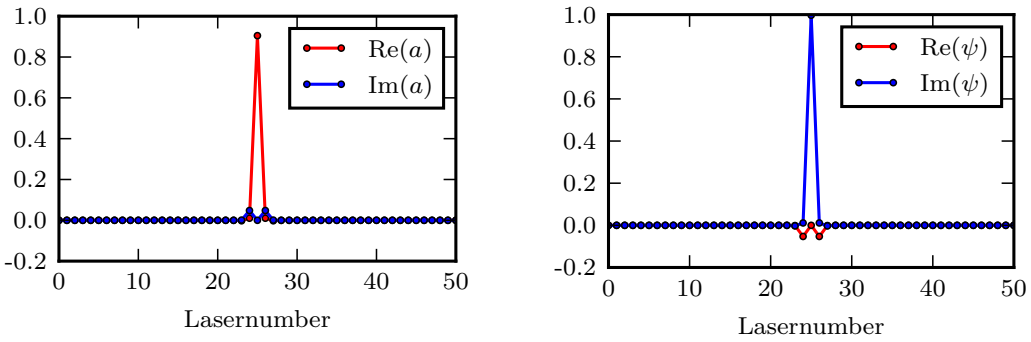

Figure 19: In the left graph the real and imaginary part of the solution in fig. 9b is plotted. The right image shows the eigenfunction of the neutrally stable eigenvalue $\lambda = 0$ which can be seen in the respective spectrum of eigenvalues in fig. 17.

One finds that $\mathrm{Re}(\psi_j) = -\mathrm{Im}(a_j)$ and $\mathrm{Im}(\psi_j) = \mathrm{Re}(a_j)$ (besides some scaling factors which is present due to the normalisation of the eigenvectors). To examine this finding in more detail we separate the phase from the amplitude: $a_j(t) = b_j e^{i\varphi}$ where $b_j \in \mathbb{R}$ is the time-invariant amplitude and φ is the phase. Interestingly, when considering the derivative with respect to the phase φ it leads to the previous observation:

$$\frac{\partial a_j}{\partial \varphi} = i b_j e^{i\varphi} = i a_j \tag{65}$$

$$= -\mathrm{Im}(a_j) + i\mathrm{Re}(a_j) \tag{66}$$

$$= \psi_j. \tag{67}$$

Therefore, one can conclude that the neutrally stable eigenvalue describes the phase shift symmetry which is present in the analysed system.

4.7. Snaking branches and two parameter continuation

So far, we have observed that for one set of parameters different solutions for DLSs consisting of different numbers of lasing laser exist with each solution having its own separate branch in the bifurcation diagram (see fig. 14). However, when other parameters are altered, e.g., the line width enhancement factor α, the behaviour can change. For example for $\alpha = 0.8$ a so-called snaking bifurcation structure was found (see fig. 20).

Now, the interesting question is, how the branches in fig. 14 transformed into the snaking structure in fig. 20. In order to examine this transition, we conduct a *two parameter continuation*. First of all, we plot bifurcation diagrams for different α and track the position of the different bifurcation points (Hopf and fold bifurcations). One finds that the snaking structure only exists for (approximately) $\alpha \in [0.25, 0.817]$ (other parameters as in fig. 20). For smaller and larger values separate branches for the one and three laser solutions exist. For a better visualisation of the dynamics with a smaller step size in α see the animation `snaking-dynamics.mp4` in appendix A.

Starting from $\alpha = 0$ (see fig. 21) one can see that the bifurcation diagram resembles fig. 14. There is a Hopf bifurcation H_1 for the one laser DLS which occurs just before G_{th} and around the main fold of the three DLS solution $\mathrm{F}_{m,3}$ two additional Hopf bifurcation appear. When α is increased H_1 drifts towards smaller values of G_0 (see $\alpha = 0.15$ in fig. 21) which means that the interval for a stable solution becomes smaller. For a further increase to $\alpha = 0.18$ a new feature on the branches appears. On both branches, consisting of a one and a three lasing laser DLS, two folds form. For $\alpha = 0.245$ (marked with F_1, F_2, C_1 and C_2) they drift away from each other and form a curl (three lasing laser DLS) and a snaking structure (one lasing laser DLS). Additionally, the Hopf bifurcation on the branch describing a one lasing laser DLS has disappeared. A linear stability analysis reveals that this branch is stable between $\mathrm{F}_{m,1}$ and H_1. The branch consisting of three lasing lasers on the other hand is mostly unstable. Only a small section between the Hopf bifurcations around the main fold and the curls is stable. The stability changes in an additional bifurcation point which will be object of further analysis in section 4.9.

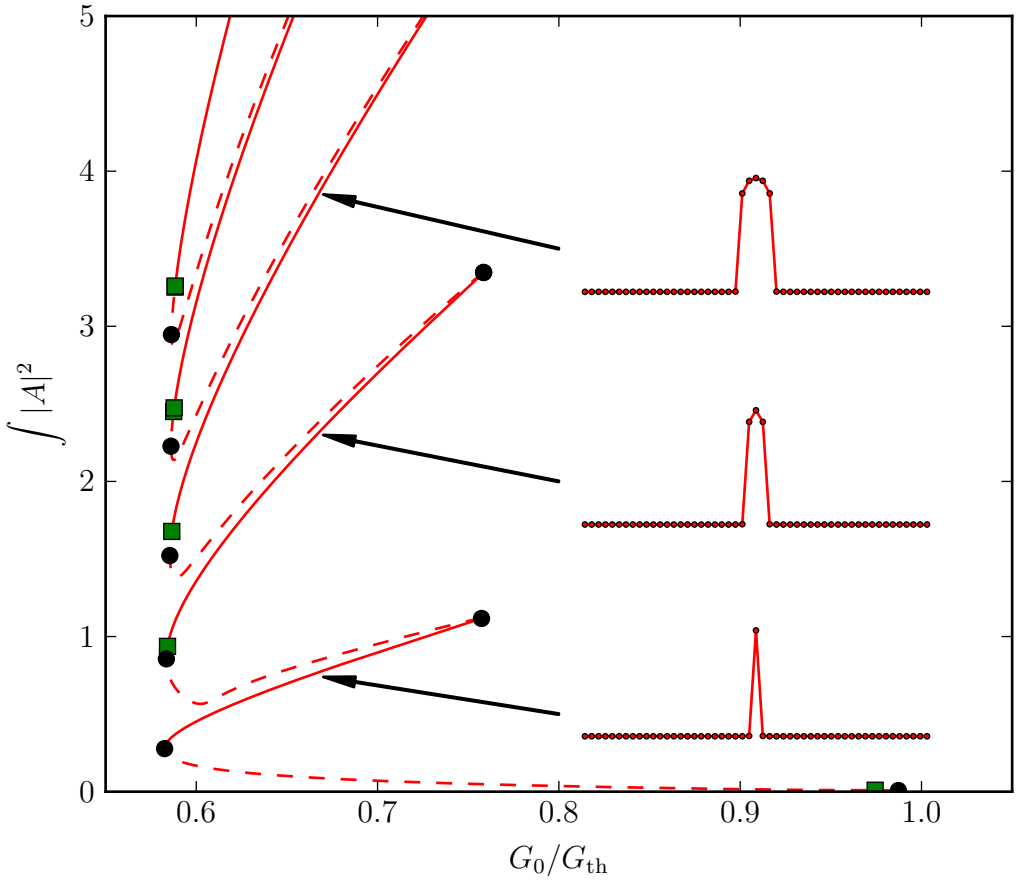

Figure 20: For the parameter set $(Q_0, \alpha, \beta, c, d, s, \kappa = 0.3, 0.8, 0.5, 0.004, 0, 30, 0.8)$ a snaking structure occurs where the stable branches for the one, three, five, etc laser DLS (solid line) are connected by unstable branches (dashed line). In appendix A there is an animation which illustrates the solution profiles along the branch (`alpha080-solutions-along-branch.mp4`).

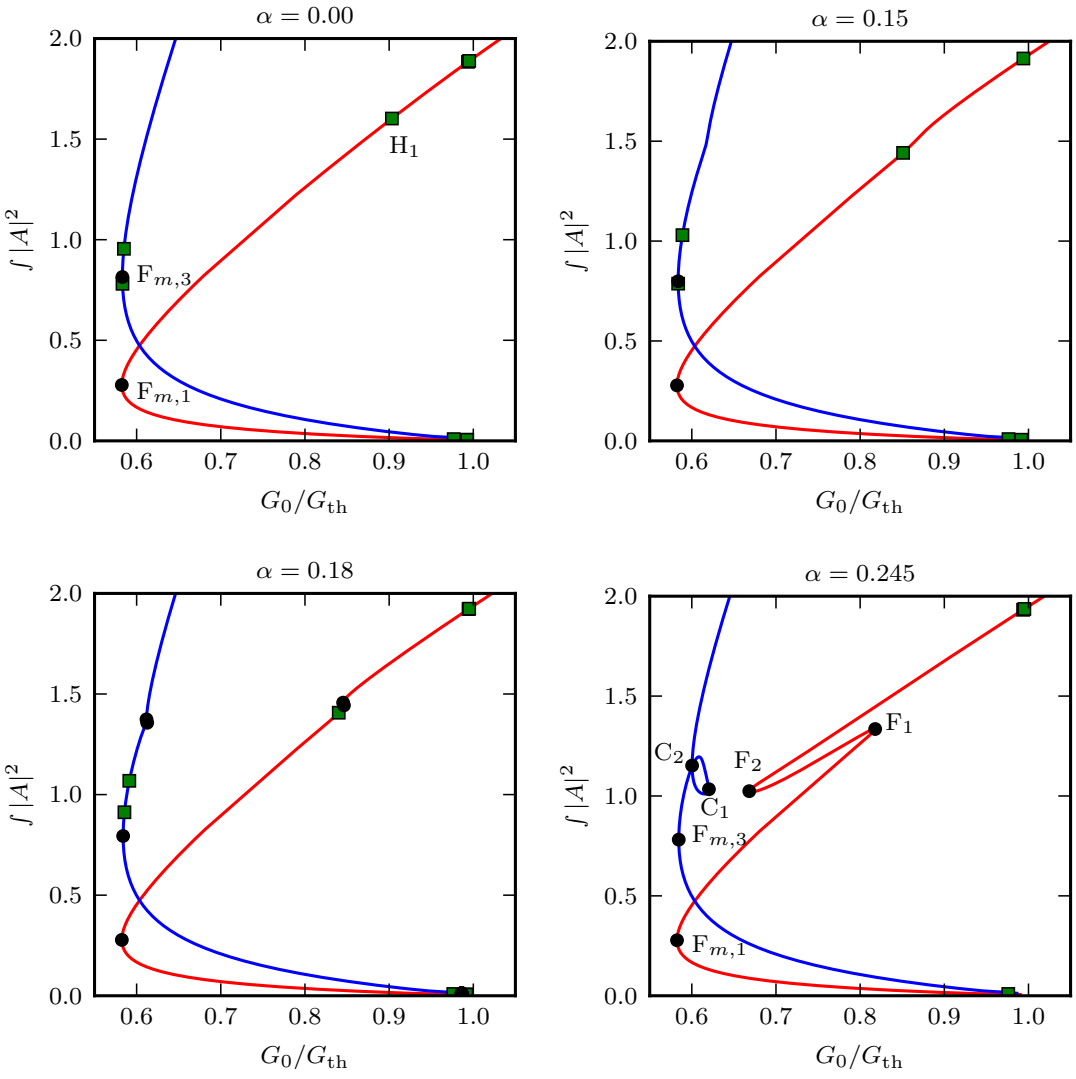

Figure 21: Bifurcation diagrams for small values of α, other parameters as in fig. 20. The red line denotes the branch consisting of a one lasing laser DLS while the blue line stands for three lasing lasers. The labels are displayed for references.

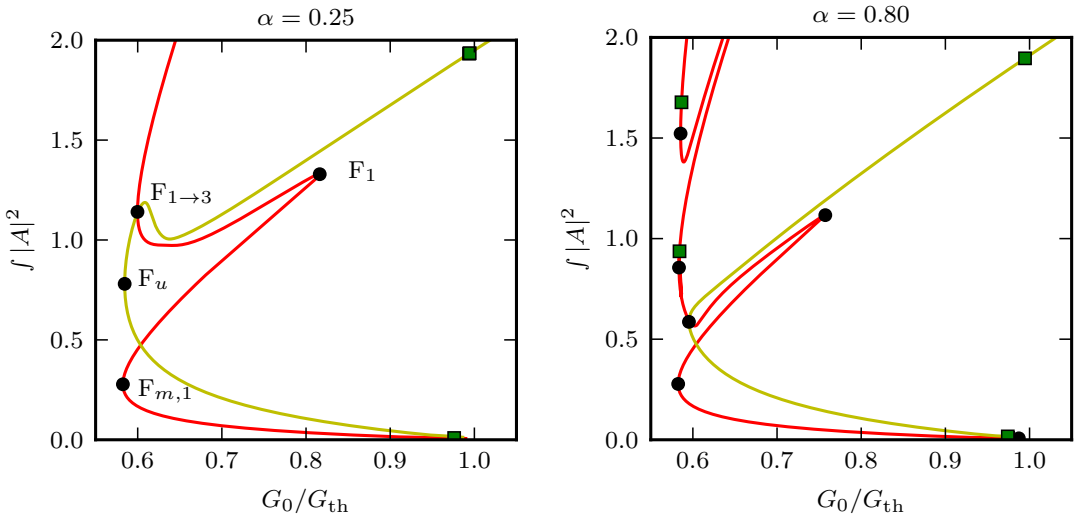

Figure 22: Bifurcation diagrams for values of α for which branches are connected by a snaking structure (red line), other parameters as in fig. 20. The stability of the branch behaves analogously to fig. 20. The yellow branch connects the unstable parts of the one and three laser DLS which existed before the snaking structure emerged. It is unstable for all values of G_0.

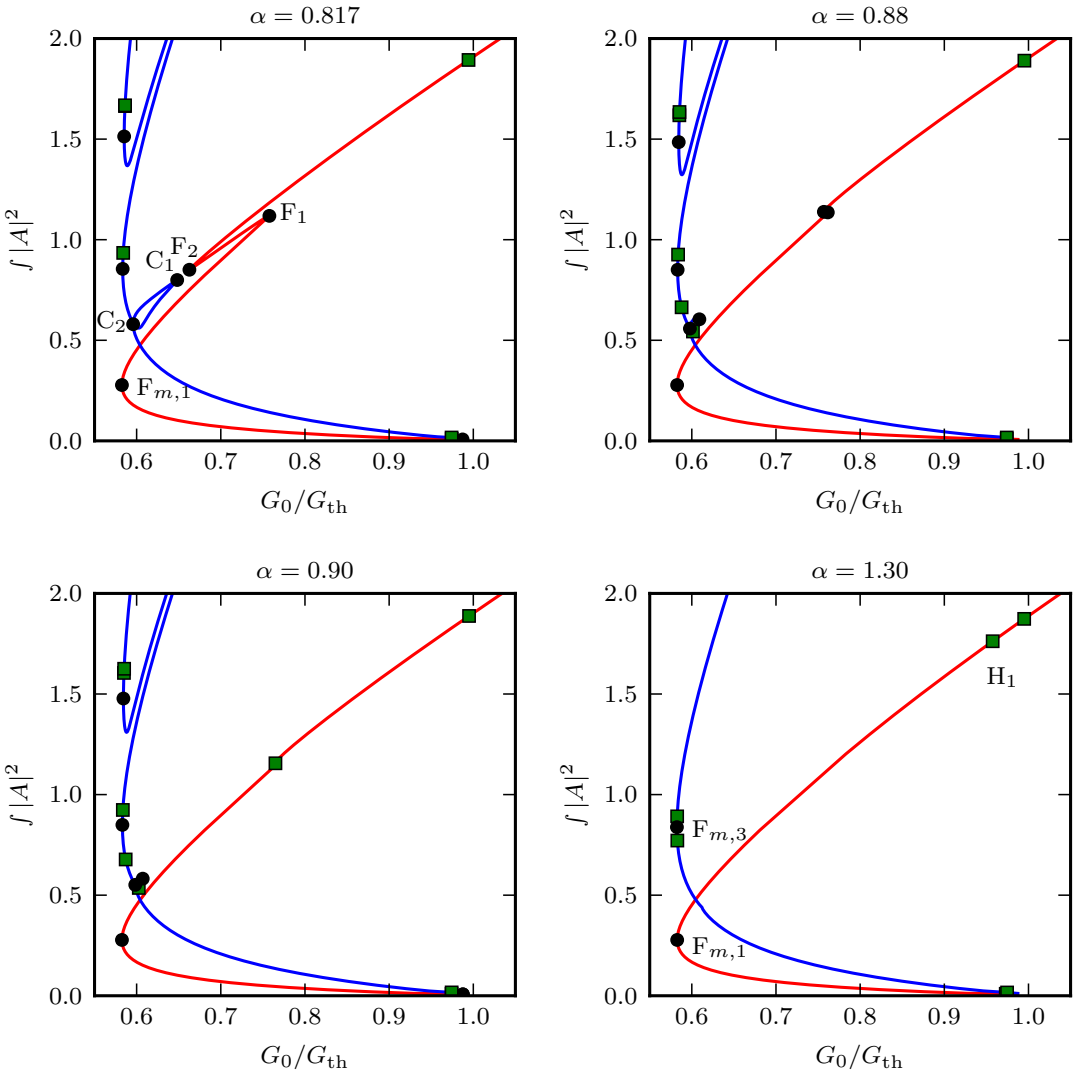

Figure 23: Bifurcation diagrams for larger values of α, other parameters as in fig. 20. The red line denotes the branch consisting of a one lasing laser DLS while the blue line stands for three lasing lasers. The labels are displayed for references.

In fig. 22 one can see that compared to $\alpha = 0.245$ in fig. 21 two folds collided and now $F_{1\to3}$ forms the link between the stable parts of the two branches. Also, the unstable branches fused (yellow line) and conclusively form a branch which looks like a three laser DLS until the main fold F_u and then transforms into an one laser DLS. The whole branch is unstable.

A further increase in α results in a separation of the two branches (see fig. 23). Like in fig. 21 a curl on the three laser branch evolves (C_1 and C_2) but in contrast to small α it is located on the opposite side of the fold. When α is increased the curl becomes smaller until it disappears after all. The same happens to the snaking structure on the branch consisting of one lasing laser DLS (F_1 and F_2). The two folds move closer to each until they collide the Hopf bifurcation H_1 is initiated. For $\alpha = 0.817, \alpha = 0.88$ and $\alpha = 0.90$ the three laser solution is still connected to the five laser solution, indicating that the previously described dynamics also apply to solutions with multiple lasing lasers. Only the threshold values for α for which the branches change differ. In contrast to the similarly looking branches for small values of α the three lasing lasers DLS are indeed stable. The whole process of connecting and disconnecting the branches can be understood as a transcritical transition.

To sum up the findings for the different α we track the bifurcation points (folds and Hopf bifurcations) on the two parameter plane (α, G_0) (see fig. 24). In order to comprehend the plot let us start at $\alpha = 0$ and then move towards larger α. First of all one notices that the main fold's location for the one lasing laser DLS $F_{m,1}$ doesn't change significantly with α while the main fold on the three lasing lasers branch $F_{m,3}$ does. The first feature which appears are the folds in the curl on the three lasing lasers branch (C_1 and C_2 in fig. 21). Intuitively their starting point is a so called *cusp*, a point in the two parameter plane where two branches are initiated. For slightly larger α also F_1 and F_2 start in a cusp. The Hopf bifurcation H_1 on the one lasing laser branch coexist with the folds but merges with them for larger alpha. In fig. 22 we saw that the one and three lasers DLSs get connected and form a snaking bifurcation structure. On the two parameter plane this is represented by another cusp from which the folds F_2 and C_1 start. Simultaneously, C_2 turns into $F_{1\to3}$ and the main fold of the three lasing lasers branch $F_{m,3}$ becomes the main fold of the unstable branch F_u. Now we're in the interval for α where snaking occurs. The branches get separated again when F_2 and C_1 start from a cusp at around $\alpha = 0.817$ (see fig. 23). At a certain point

$F_{1\to3}$ turns into the main fold of the three lasers DLS $F_{m,2}$ and the main fold of the unstable branch becomes a fold (C_2) in the curl on the three lasing lasers branch. With increasing α the folds F_1 and F_2 drift towards each other until they collide and form the Hopf bifurcation H_1 on the one lasing laser branch. Also the curl on the three lasing lasers branch shrinks which is why C_1 and C_2 origin in another cusp.

Generally, we can see that the range of stability changes on the two-parameter plane for both the one and three lasing laser DLS. In particular for the one lasing laser DLS, the range of stability is confined by the main fold on the left side and the Hopf bifurcation H_1 and the fold F_1, respectively, on the right side. Thus, in fig. 24 one can see that starting from $\alpha = 0$, the range of stability decreases until $\alpha \approx 0.7$. Then F_1 drifts towards larger values of G_0 such that the range of stability increases. This is only partly compatible with the results in [GJ17] where it was found that the range of stability constantly increases with α.

The analysis in this chapter was limited on the transition between the one and three lasing laser DLSs. But as fig. 23 suggests there is also a transition between the three and five, five and seven lasing laser DLS, etc. Furthermore, fig. 25 shows that snaking bifurcation branches for DLSs consisting of an even number of lasing lasers exist as well.

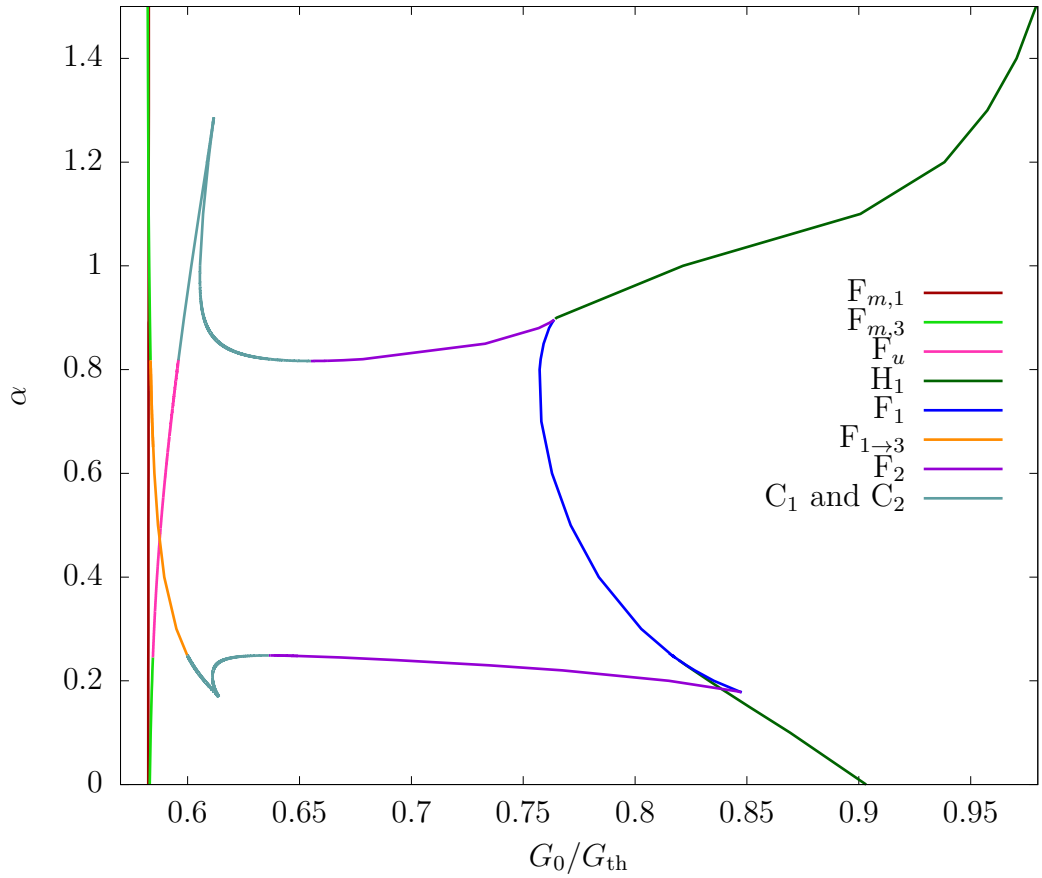

Figure 24: Behaviour of important branch points on the two parameter plane α-G_0, other parameters as in fig. 20. The names in the legend refer to the annotations in figs. 21 to 23. The plot was created by a mix of computing the branches for different values of α discretely and using the two-parameter-continuation feature in `AUTO-07P` which can track the movement of folds and bifurcation in the two parameter plane (but is not always reliable to use).

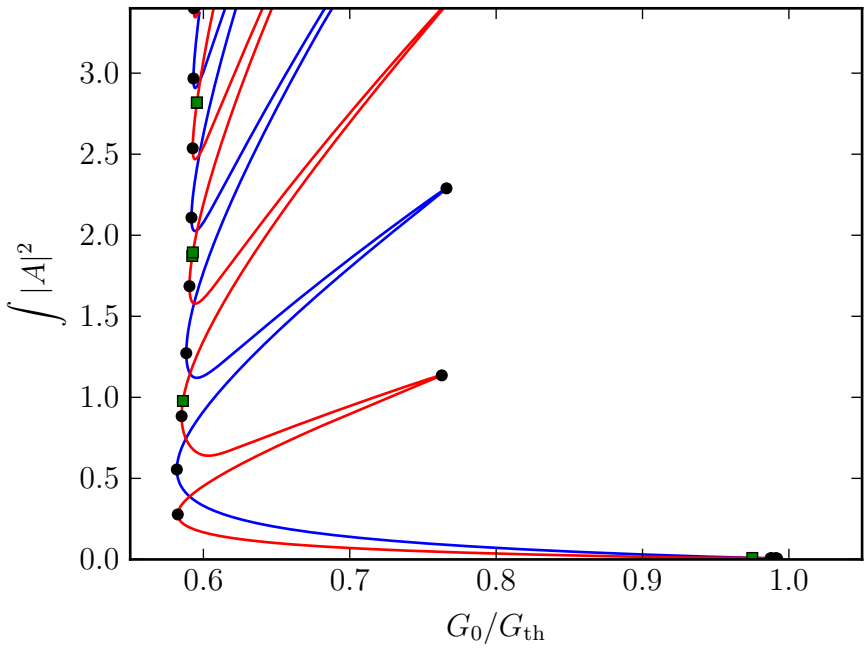

Figure 25: Bifurcation diagram for snaking branches for DLSs consisting of an even (blue) and odd (red) number of lasing lasers. $\alpha = 0.6$, other parameters as in fig. 20.

4.8. Continuation in c

In eq. (9) the coupling c was introduced which is necessary for the discretisation of the system. It has been kept constant to $c = 0.004$ up to this point. For $c \to \infty$ the system is expected to behave as in the continuous case but at first we will stick to small couplings and analyse its influence on the system. In fig. 26 branches for different couplings are visualised.

For very small couplings up to $c = 0.003$ one notices that the Hopf bifurcation which normally occurs before G_{th} (e.g. labeled with H in fig. 14) is not present. It firstly appears for $c = 0.004$. Then, for a further increase in c the Hopf bifurcation drifts towards smaller values of G_0. This dynamic resembles the continuation in the linewidth enhancement (see fig. 21) where smaller values for α pushed the Hopf bifurcation towards smaller values of G_0 as well and thus, decreasing the range of stable DLSs.

Furthermore, the Hopf bifurcation splits into two separate Hopf bifurcations for $c \in [0.0070, 0.0095]$. This is possible because in fig. 17 it was observed that for $c = 0.004$ four eigenvalues cross the imaginary axis at the Hopf bifurcation making it a double Hopf bifurcation. For the mentioned interval, these pairs of eigenvalues simply separate from each other and change their sign one after the other (see fig. 27). One notices that one eigenfunction is odd (fig. 27b) while the other is even (fig. 27c).

Next, for $c = 0.01$ two folds replace the Hopf bifurcations on the branch (see fig. 26b). The appearance of the folds is again a similar behaviour to what has been observed for dynamics when altering α (see fig. 21). Conclusively, for even larger couplings a snaking bifurcation structure appears (see fig. 26c) which connects the branch of the one lasing laser DLS to the branches of DLSs with more lasing lasers. However, stable DLSs are only given for a small parameter range around the main fold. Most parts of the snaking branches are unstable due to the large coupling.

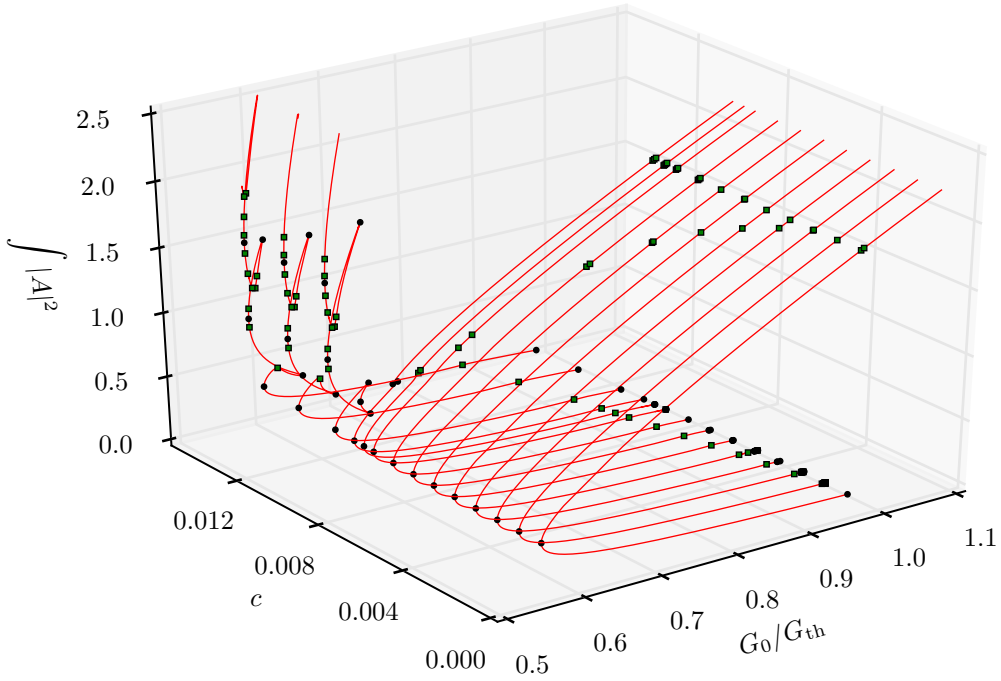

(a) Evolution of the branches for a continuation in G_0 for different values for the coupling c.

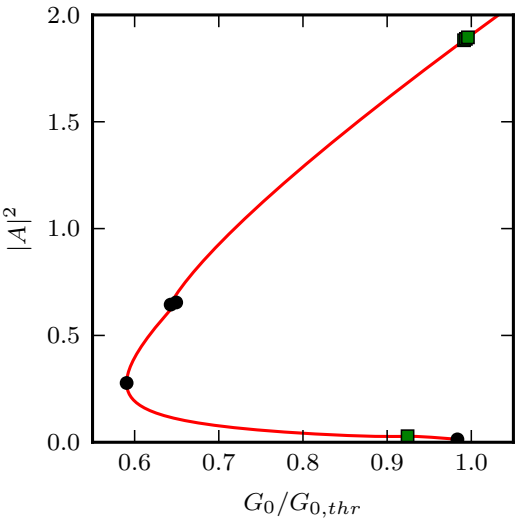

(b) $c = 0.010$

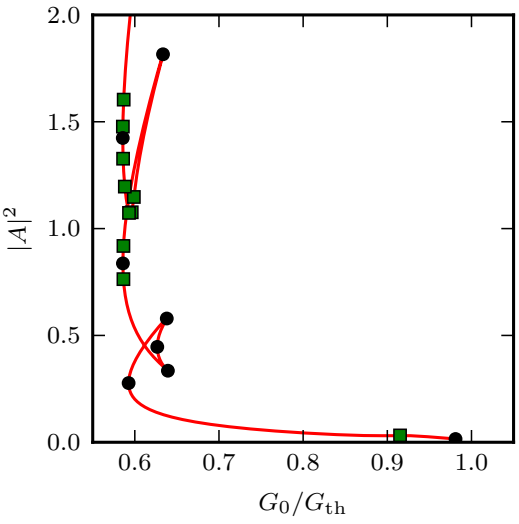

(c) $c = 0.011$

Figure 26: Bifurcation diagrams for different values of c. Other parameters are $(Q_0, \alpha, \beta, d, s, \kappa = 0.3, 1.5, 0.5, 0, 30, 0.8)$. The branches all belong to DLSs consisting of one lasing laser. In figs. 26b and 26c two branches are displayed separately for a better readability. Figure 26a shows branches in G_0/G_{th} for different $c \in [0.001, 0.015]$. The green squares denote Hopf bifurcations while the the black dots stand for folds.

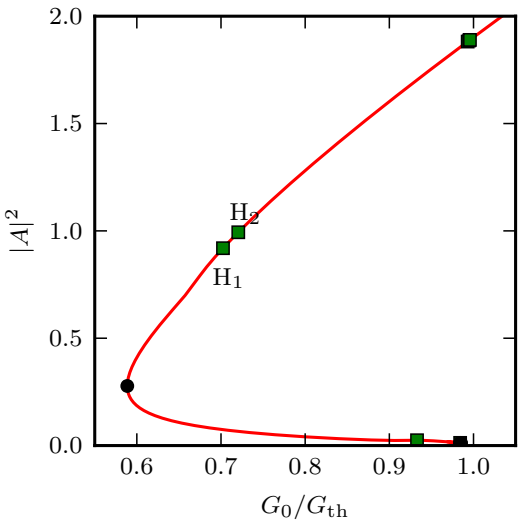

(a) Bifurcation diagram in G_0 for $c = 0.009$

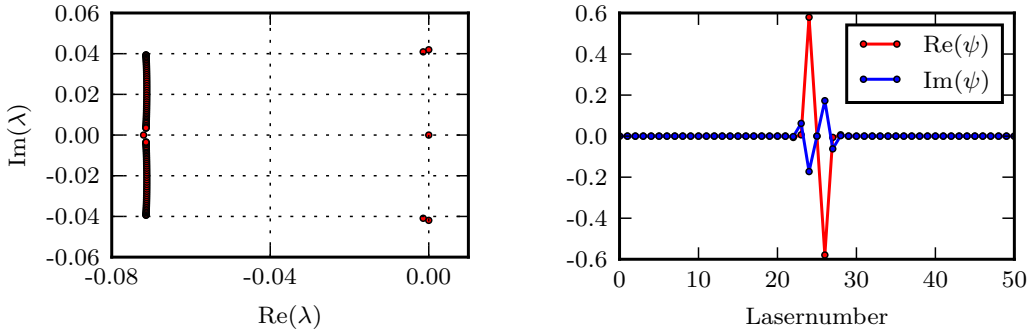

(b) Spectrum of eigenvalues at the Hopf bifurcation H$_1$ (see (a)) and according eigenfunction

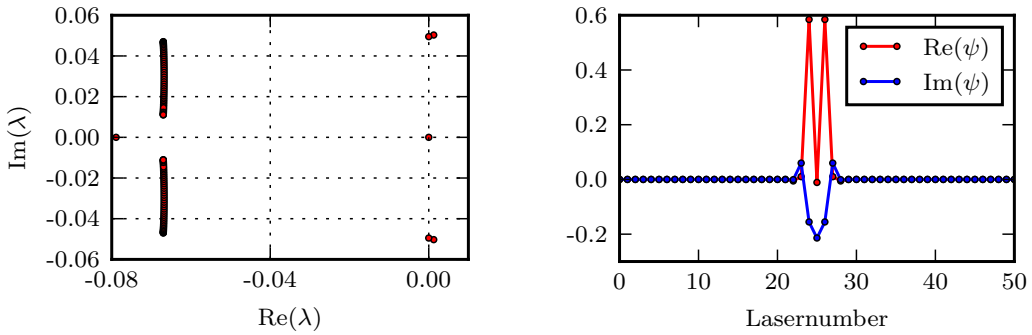

(c) Spectrum of eigenvalues at the Hopf bifurcation H$_2$ (see (a)) and according eigenfunction

Figure 27: Separation of the double Hopf bifurcation into two separate Hopf bifurcations.

4.9. Unsymmetrical solution branches

So far, all observed DLSs were symmetrical. Indeed, this is to be expected as the differential equation doesn't differentiate or favour any direction. However, unsymmetrical solution profiles were observed with some of them even being stable. When analysing the stability for the three laser solitons for small values of α (see fig. 21) it was found that the stability changes along the branch which means that some kind of bifurcation must occur (see fig. 29). Its exact location was tracked down with a linear stability analysis (see fig. 30). From here it was possible to follow both paths with numerical continuation. The branch which splits of from the main "symmetrical" branch exhibits the mentioned unsymmetrical solution profiles which are displayed in fig. 28.

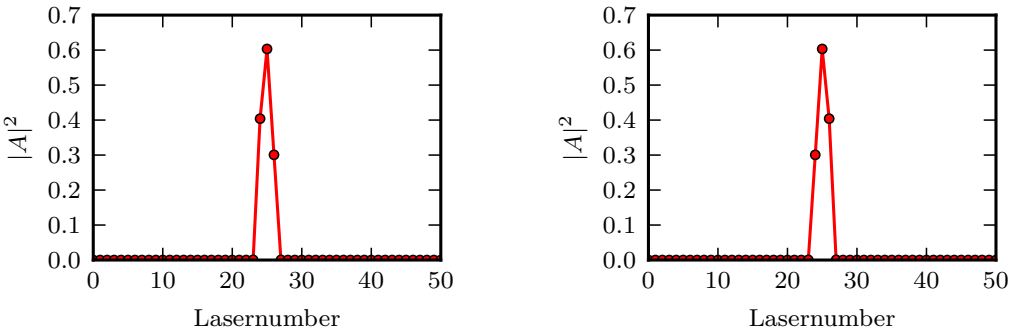

Figure 28: The two unsymmetrical solution profiles at the Hopf bifurcation marked with H in fig. 29.

In fig. 29 one notices that the main branch is stable for only a very small interval in G_0. The stability on the main branch changes in a bifurcation from where a branch of unsymmetrical solution profiles emerges. However, its stability rapidly changes in a Hopf bifurcation. Indeed, the "unsymmetrical" branch exists twice as the asymmetry can evolve in both directions from the central laser. The two according solution profiles are displayed in fig. 28. Figure 30 shows the spectrum of eigenvalues around the bifurcation point. One sees in fig. 30b that there are two eigenvalues $\lambda = 0$, one of them is the neutrally stable eigenvalue, the other denotes the bifurcation. The eigenvalue can either drift towards a positive real part (fig. 30c) which means the branch becomes unstable or the real part becomes negative such that the branch is stable until two eigenvalues change signs at a Hopf bifurcation (fig. 30d).

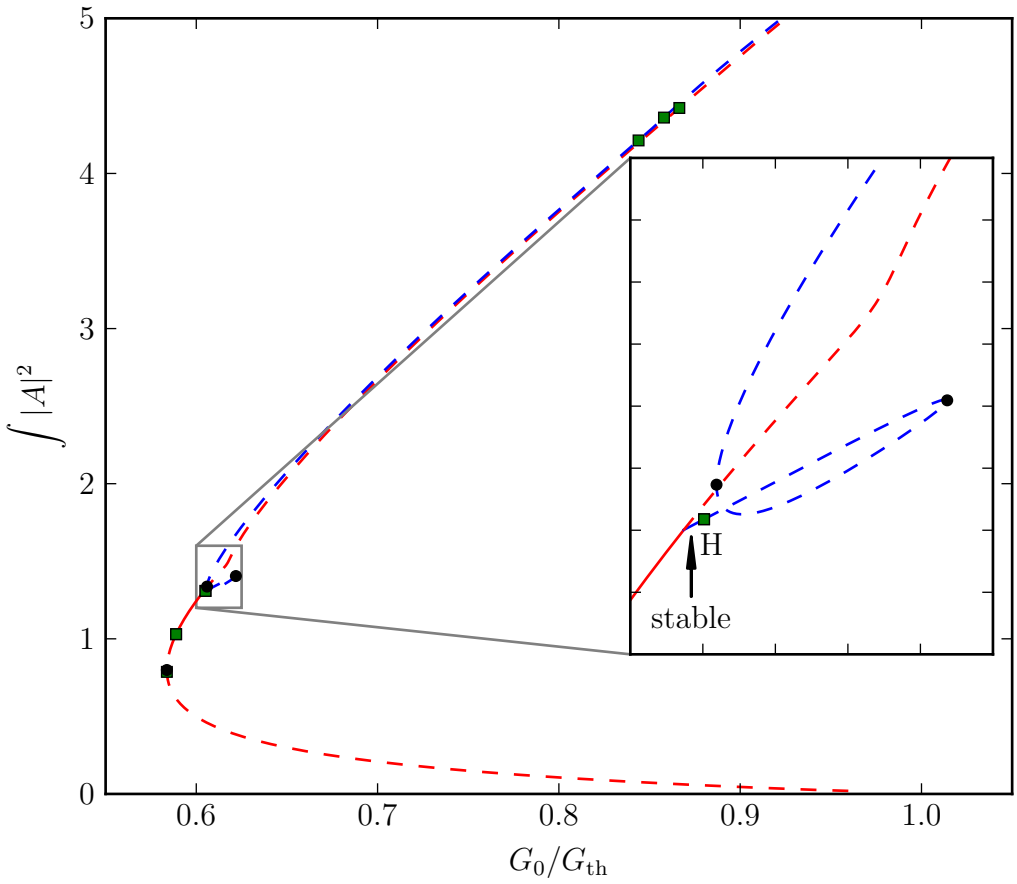

Figure 29: Branches for DLSs consisting of three lasing lasers, the used parameters are $(Q_0, \alpha, \beta, c, d, s, \kappa = 0.3, 0.15, 0.5, 0.004, 0, 30, 0.8)$ (same as in fig. 21). The red line denotes the branch of symmetrical solution profiles while the solution profiles on the blue branch are unsymmetrical. Solid branches are stable and dashed ones are unstable.

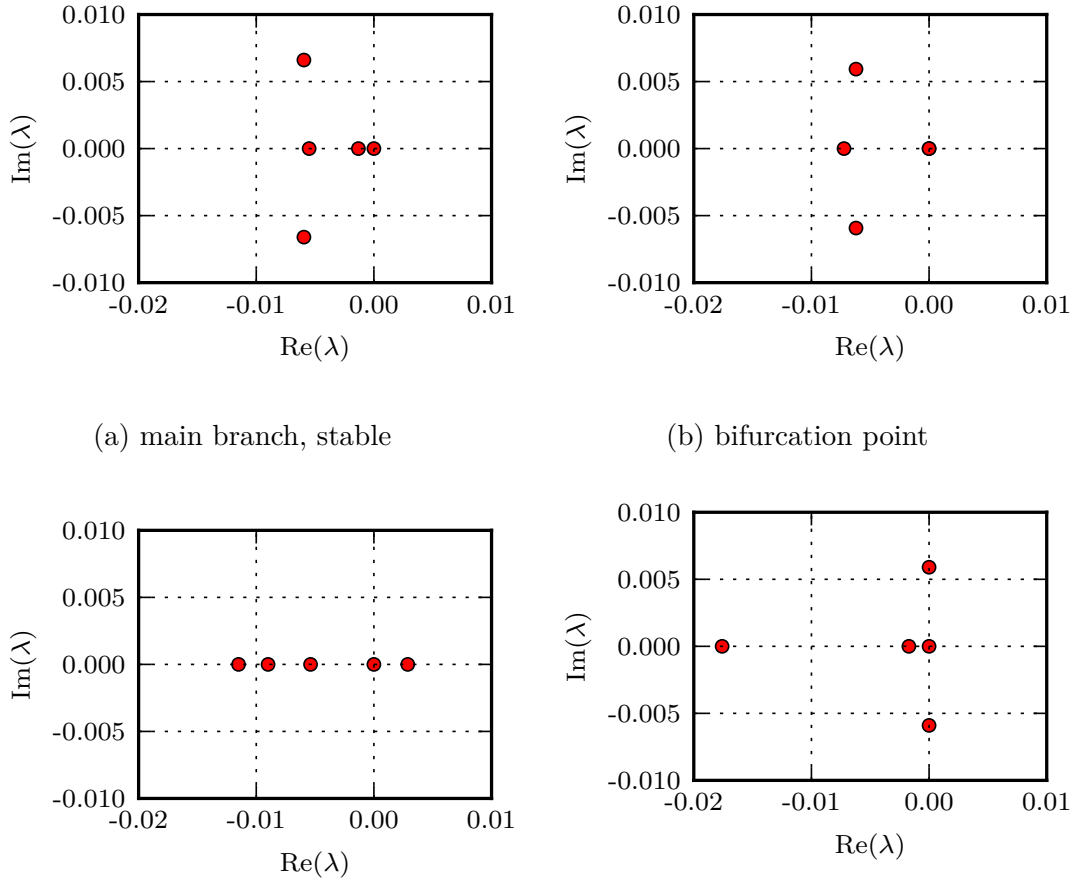

(a) main branch, stable

(b) bifurcation point

(c) main branch, unstable

(d) at the Hopf bifurcation H on the branch of unsymmetrical solution profiles

Figure 30: Spectrum of eigenvalues at different points around the bifurcation point in fig. 29. The plots are all zoomed in such that they just show the crucial eigenvalues.

The important question is why the unsymmetrical solitons exist or rather what triggers their existence. This can be explained with regard to the eigenfunction which triggers the mentioned bifurcation (see fig. 31). One sees that the eigenvectors look similar to the derivative of the solution profile. This type of modes is referred to as *Goldstone mode*.

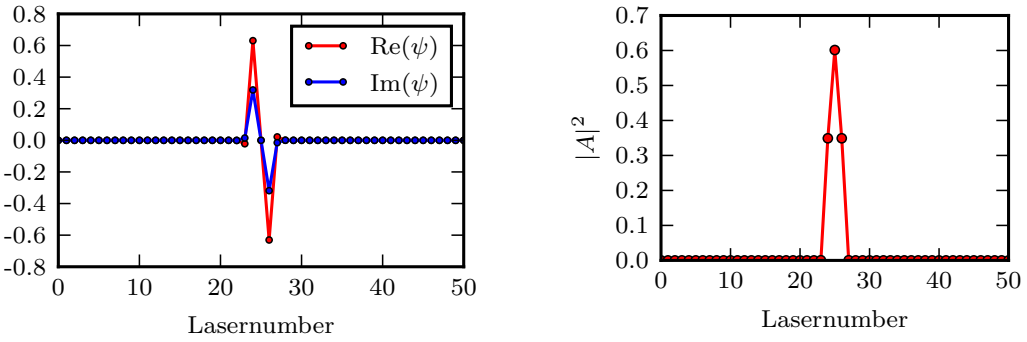

(a) eigenvector (b) solution profile

Figure 31: Figure 31a shows the eigenvectors of the bifurcation point in fig. 29, fig. 31b displays the according solution profile.

Let us look at the continuous case for a moment and regard a small shift of δ. This can be approximated by $A(x+\delta) = A(x) + \delta\partial_x A(x)$. Here, the derivative occurs again, such that one can conclude that the existence of the eigenvector triggers the "shift" or rather asymmetry. However, it was not possible to trigger a "real" shift in form of a drifting soliton for this set of parameters. Drifting solitons are addressed again in section 4.10.

As a small remark it is worth mentioning that obviously, the here presented asymmetry can't exist for a soliton with one lasing laser which is why for the respective branches a according bifurcation doesn't occur. Conclusively, the branch for the minimal soliton is stable for a much larger interval in G_0 than the three laser soliton is.

4.10. Drifing solitons

So far, all regarded DLSs were stationary in a sense that their amplitudes were fixed to the laser where the soliton was initialised. However, in previous work discrete *drifting* or *walking solitons* have been observed [EL13; EPL05; ELS07]. Indeed, for a continuous system this can be explained easily with the presence of translational symmetry which needs to be broken by writing solutions in the form $E(x,t) = A(\xi,t)e^{i\omega t + i\omega\xi/2}$ where $\xi = x - vt$ and v is the velocity of the translational movement [Vla+97]. However, for discrete systems translation symmetry is not present and thus, for smaller couplings solitons are "trapped" by discreteness and rest unless the driving force exceeds some critical value [ELS07]. It was found that for large couplings the critical value is inversely proportional to the coupling parameter [EPL05].

Hence, the next step in the analysis is to consider even larger couplings c. At some point numerical inaccuracies would be sufficient as a driving force but in order to accelerate the process in each step in direct numeric noise in form of random numbers is added to the solution. In figs. 32 and 33 examples for drifting solitons are displayed. The spectrum of eigenvalue in fig. 32c is much more complex than for the nondrifting solitons. However, fig. 32d reveals that similarly to the case of unsymmetrical solution profiles (see section 4.9) a Goldstone-like mode exists which can trigger the translation. This mode belongs to a Hopf bifurcation. Many other pairs of complex conjugated eigenvalues exist as well which leads to the to the complex dynamics of the translation which can be best observed in the complementary animation `drifting-bright-soliton` (see appendix A).

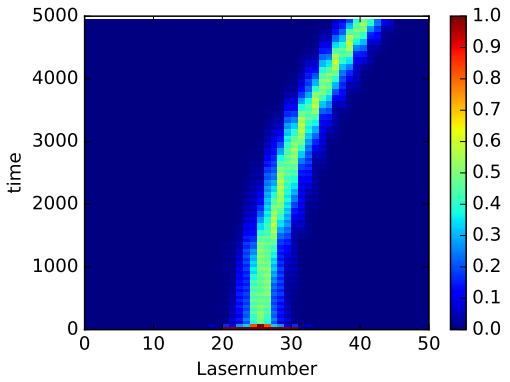

(a) Time evolution of a drifting soliton.

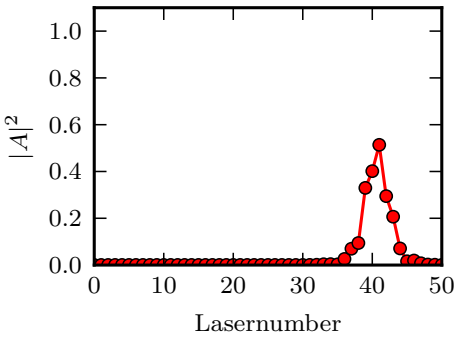

(b) Solution profile of the last step of the time simulation.

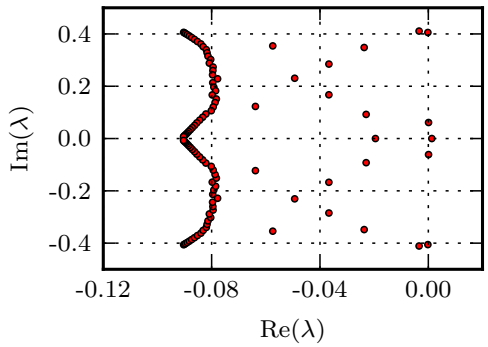

(c) Spectrum of eigenvalues

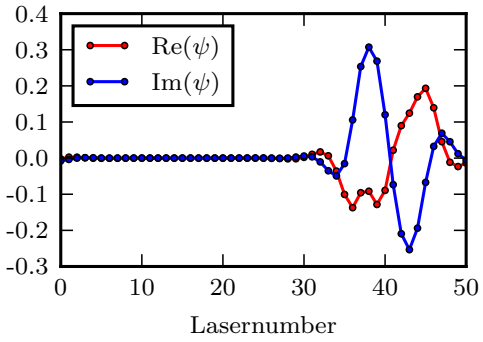

(d) Goldstone-like mode.

Figure 32: The used parameters are $(G_0, Q_0, \alpha, \beta, c, d, s, \kappa = 0.33, 0.3, 1.5, 0.5, 0.1, 0, 30, 0.8)$. The amplitude of the noise is $8 \cdot 10^{-5}$. The initial condition is $\mathrm{Re}(A_j) = 1$ for the eleven central lasers.

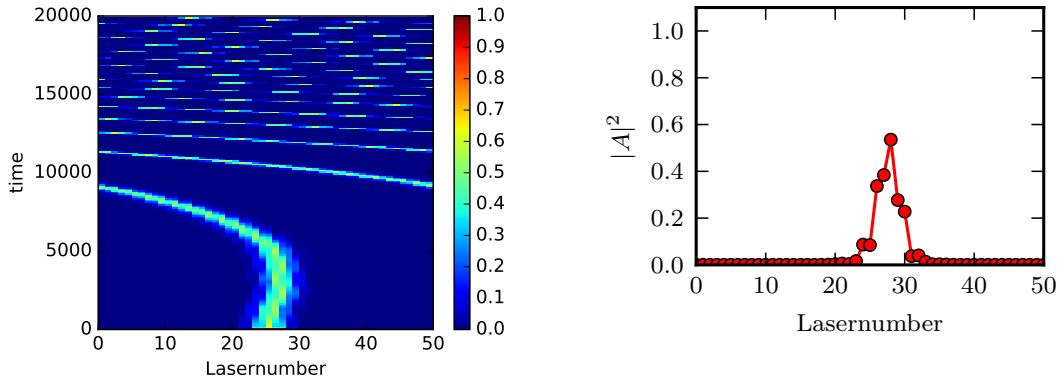

(a) Time evolution of a drifting soliton.

(b) Solution profile of the last step of the time simulation.

Figure 33: Same parameters as in fig. 32abut the initial condition is $\mathrm{Re}(A_j) = 1$ for the five central lasers. First of all one sees that the profile of the soliton as in fig. 32a even though the initial condition was much smaller. Hence, it seems that there need to be a certain number of lasing lasers for high couplings for a soliton to exist. This hypothesis is supported that for $n \leq 3$ lasing lasers no soliton forms. Next, one sees that the soliton changes the direction of movement while drifting at the beginning. Furthermore, the soliton accelerates with time as the translastion becomes faster and faster. The same long term behaviour was observed for the soliton in fig. 32.

Up to this point all regarded solitons were *bright* solitons, meaning that they are realised by a localised maximum in intensity. However, also *dark* (or *grey*) solitons exist. These solitons are defined by a localised minimum in intensity and have been observed in previous work [EPL05; YCS08]. Like their bright counterpart they are also able to drift. They occur in the analysed model as well for parameter sets very similar to those of the drifting solitons in figs. 32a and 33a only differing in the gain value G_0. Figure 34 shows a drifting dark soliton.

In fig. 34a one can see that in the initial phase of the time evolution - because of the strong coupling c and large gain G_0 - more and more lasers become lasing until all except for one are lasing. This state stays stationary until the "hole" spontaneously starts to move which happens with a constant velocity. The velocity indeed remains constant which was checked by a direct numerical continuation for a much longer simulation time. The movement is realised by switching between one (fig. 34c) and two (fig. 34d) non lasing lasers. Furthermore, one sees that the intensity profile is not symmetric. On the right side of the non lasing laser(s) the profiles in figs. 34c and 34d show oscillatory foothills. These can lead to bounded states between two dark solitons and thus, molecule-like structures could potentially be realised. Generally, the drift follows a different mechanism than the drifting bright soliton as the eigenvalue spectrum in fig. 34b differs from that in fig. 32c. Instead of Hopf bifurcation real eigenvalues appear which must trigger the translation.

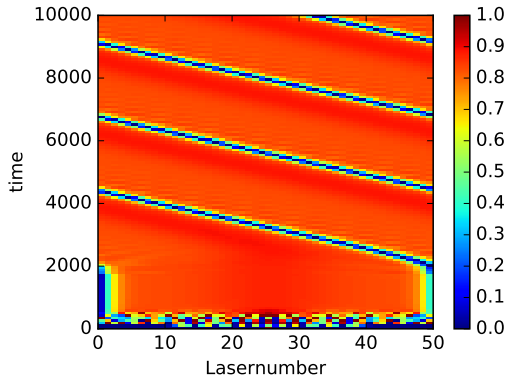

(a) Time evolution of a drifting dark soliton

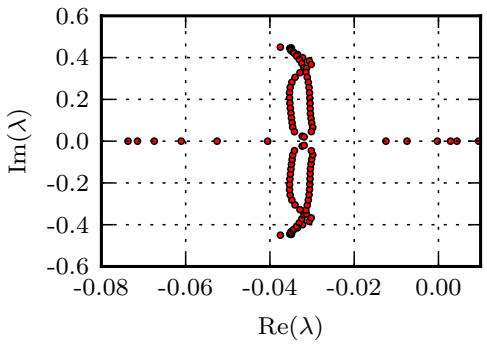

(b) Spectrum of eigenvalues

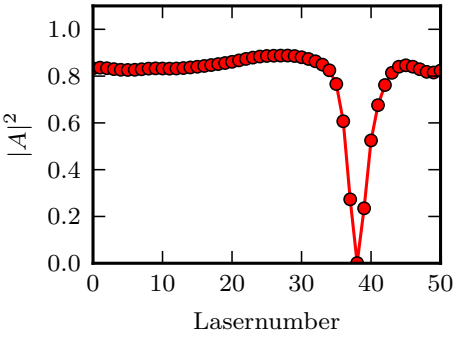

(c) Solution profile of a dark soliton with one non lasing laser

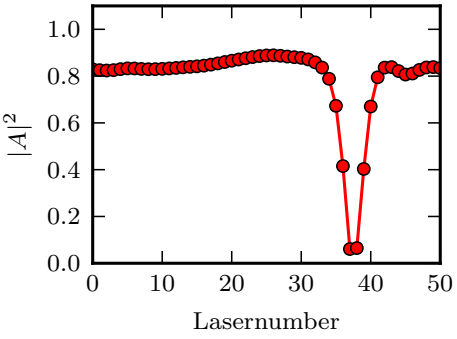

(d) Solution profile of a dark soliton with two non lasing lasers

Figure 34: The used parameters are $(G_0, Q_0, \alpha, \beta, c, d, s, \kappa = 0.365, 0.3, 1.5, 0.5, 0.1, 0, 30, 0.8)$, the initial state is a single lasing laser, no noise was added.

5. Conclusion and Outlook

In conclusion, based on the continuous description of the transverse dynamics of light bullets in [GJ17], we have created a discretised one-dimensional version of this simplified model by descretising the transverse Laplacian. Instead of having to solve a PDE we have transformed the problem to a set of complex coupled first order ODEs. This initial value problem can be solved by simple numerical methods such as the forth order Runge-Kutta methods which was used for this theses. In order to analyse the behaviour of the system to changes in different parameters a numerical continuation was realised with the program `AUTO-07P`. The stability along the branches was determined with a linear stability analysis.

First of all, numerical simulations confirmed the existence of stable discrete solitons for the given model. It was observed that depending on the initial state DLSs which cover different number of lasing lasers evolved. This shows the existence of multistabilities in the system. Another finding was, that even though it seemed as $A_j = 0$ for all non lasing lasers, A_j increases exponentially towards the lasing lasers.

Next, by considering small perturbations to $A_j = 0\ \forall j$ it was found that the threshold gain G_{th} from which on all branches are unstable can easily be computed for a given set of parameters: $G_{\text{th}} = \frac{2}{\sqrt{\kappa}} + Q_0 - 2$. On the bifurcation diagram the G_{th} was indicated by a Hopf bifurcation at which many eigenvalues crossed the imaginary axis at once.

The fixed points obtained from the direct numerical simulation were only stable in $\int |A|^2$ but not separately in the real and imaginary parts of A_j which are both oscillating with a constant carrier frequency ω. This indicates the phase shift symmetry of the system. In order to use the results of direct numerics as initial states for the numerical continuation this symmetry was needed to be broken which can be achieved with the ansatz $A_j = a_j e^{i\omega t}$ where a_j is the time independent amplitude. Conclusively, the ODEs can be rewritten for a_j which leads to ω appearing in the equations. However, the carrier frequency can be computed for any given stable state.

Now that all the necessary preparatory work for the numerical continuation was done, the gain value G_0 was used as the primary control parameter. It was found that for the parameter set $(Q_0, \alpha, \beta, c, d, s, \kappa = 0.3, 1.5, 0.5, 0.004, 0, 30, 0.8)$ separate branches for DLSs consiting of different numbers of lasing lasers exist. The main features of the branch consist of a Hopf bifurcation at $G_0 = G_{\text{th}}$,

another Hopf bifurcation just before G_{th} and a fold which connects the unstable low power solutions with the stable high power branch. Depended on the number of lasing lasers additional Hopf bifurcations occur around the fold.

For different values for the line width enhancement factor α the behaviour of the branch changed. With the parameters $(Q_0, \beta, c, d, s, \kappa = 0.3, 0.5, 0.004, 0, 30, 0.8)$ and $\alpha \in [0.25, 0.817]$ a snaking branch structure which connected the stable one and three lasing laser DLSs by an unstable branch. The same scheme with different threshold values for α applies for the two and four, three and five, etc. lasing laser branches. On the two-parameter-plane (α, G_0) one can see that the necessary fold bifurcations evolved from Hopf bifurcations or originated in cusps. However, for small values of α stable solitons were only given in a small interval as a bifurcation on the branches leaves them mostly unstable. To verify the findings it would be necessary to extend the bifurcation analysis to DLSs consisting of more lasing lasers. Furthermore, snaking branches were found for continuations in G_0 and α, however, also the value of the unsaturated loss Q_0 and β are candidates for the formation of snaking branches.

The branch which splits of at the mentioned bifurcation point consist of unsymmetrical solution profiles which, nevertheless, are stable for a slim parameter range. The asymmetry is triggered by a Goldstone-like mode and can - because of the symmetry - evolve in both direction.

It was observed that when altering the coupling c the resulting bifurcation diagrams resemble those for different values of α. A similar snaking structure evolved for larger couplings. However, the ranges of stable DLSs on the branches become very small for large c. Furthermore, a transition back to separate branches like it was observed for the continuation in α wasn't found. A more detailed bifurcation analysis e.g. in the two parameter plane (G_0, c) would help to understand the dynamics.

For even larger couplings bright and dark drifting solitons were found. Like for the unsymmetrical solution profiles the dynamics of the bright DLS were triggered by a Goldstone-like mode. For the dark DLSs the modes are much more difficult to interpret because almost all lasers are lasing. The next step in the analysis of the drifting solitons would be to determine their velocity and analyse which parameters influence these dynamics. With these results drifting solitons for smaller couplings could be found. Furthermore, it remains unclear if stationary dark DLSs exist because they have only been observed for large couplings and

thus, they drift.

A. Complementary Animations

In table 1 you find a list of animations which have been mentioned throughout this thesis. The animations are stored in a cloud storage and can be accessed via the link `https://drive.google.com/open?id=1nzGMhEqRv7RCXhsnLhgmRLOCBemJoiCT`.

Table 1: Complementary animations for a better visualisation of different dynamics of the system.

filename	content
`time-simulation-1-lasing-laser.mp4`	animation of the time evolution from the initial state in fig. 9a to the steady state in fig. 9b
`time-simulation-3-lasing-lasers.mp4`	animation of the time evolution from the initial state in fig. 9c to the steady state in fig. 9d
`2-lasers-phase-change.mp4`	Two lasing lasers as the initial state. Illustrates the point in time where the neighbouring lasers get out of phase.
`alpha080-solutions-along-branch.mp4`	solution profiles along the snaking branch in fig. 20
`alpha060-solutions-along-branch.mp4`	solution profiles along along a snaking branch with an even number of lasing lasers (blue line in fig. 25)
`snaking-dynamics.mp4`	animation of the transformation from separate branches of the one and three laser solution to the snaking structure (see figs. 21 to 23)
`unsymmetrical-solution.mp4`	animation along a branch from where a branch of unsymmetrical solutions splits off
`drifting-bright-soliton.mp4`	animation for a drifting bright soliton
`drifting-dark-soliton.mp4`	animation for a drifting dark soliton

References

[AA05] Nail N. Akhmediev and Adrian. Ankiewicz. *Dissipative solitons / N. Akhmediev, A. Ankiewicz (eds.)* English. Springer Berlin, 2005, xvii, 448 p. : ISBN: 9783540237822 3540233733. URL: http://www.loc.gov/catdir/enhancements/fy0813/2004114848-t.html.

[Bra+97] Massimo Brambilla et al. "Spatial Soliton Pixels in Semiconductor Devices". In: 79 (Sept. 1997), pp. 2042–2045.

[BS08] D. Botez and D. R. Scirfres, eds. *Diode Laser Arrays*. Cambridge Studies in Modern Optics No. 14. Cambridge University Press, 2008.

[Del+06] P. J. Delfyett et al. "Optical frequency combs from semiconductor lasers and applications in ultrawideband signal processing and communications". In: *Journal of Lightwave Technology* 24.7 (July 2006), pp. 2701–2719. ISSN: 0733-8724. DOI: 10.1109/JLT.2006.875948.

[Doe+07] E. J. Doedel et al. "Auto-07p: Continuation and bifurcation software for ordinary differential equations". In: (2007).

[DP06] T. (Thierry) Dauxois and 1949- Peyrard M. (Michel). *Physics of solitons*. English. Formerly CIP. Cambridge, UK ; New York : Cambridge University Press, 2006. ISBN: 0521854210 (hbk.)

[EL13] O. Egorov and F. Lederer. "Spontaneously walking discrete cavity solitons". In: *Optics Letters* 38.7 (2013).

[ELS07] O. Egorov, F. Lederer, and K. Staliunas. "Subdiffractive discrete cavity solitons". In: *Opt. Lett.* 32.15 (Aug. 2007), pp. 2106–2108. DOI: 10.1364/OL.32.002106. URL: http://ol.osa.org/abstract.cfm?URI=ol-32-15-2106.

[EPL05] O. Egorov, U. Peschel, and F. Lederer. "Mobility of discrete cavity solitons". In: *Physical Review E 72, 066603* (2005).

[GA12] Philippe Grelu and Nail Akhmediev. "Dissipative solitons for mode-locked lasers". In: 6 (Feb. 2012), pp. 84–92.

[Gen+18] Patrice Genevet et al. "Cavity Soliton Laser Based on Mutually Coupled Semiconductor Microresonators". In: (2018).

[GH83] J. Guckenheimer and P. Holmes. *Nonlinear Oscillations, Dynamical Systems, and Bifurcations of Vector Fields*. Applied mathematical sciences. Springer-Verlag, 1983. ISBN: 9787506212830. URL: https://books.google.de/books?id=GKhRPwAACAAJ.

[GJ17] S. Gurevich and J. Javaloyes. "Spatial instabilities of light bullets in passively-mode-locked lasers". In: *Physical Review A 96, 023821* (2017).

[Gur] S. Gurevich. *Runge-Kutta methods*. https://www.uni-muenster.de/Physik.TP/teaching/courses/numerical_methods_for_complex_systems_ii_ss2018.html. Lecture on numerical methods for complex systems.

[Hau00] H. A. Haus. "Mode-locking of lasers". In: *IEEE Journal of Selected Topics in Quantum Electronics* 6.6 (Nov. 2000), pp. 1173–1185. ISSN: 1077-260X. DOI: 10.1109/2944.902165.

[Jav17] J. Javaloyes. "Cavity Light Bullets in Passively Mode-Locked Semiconductor Lasers". In: *2017 European Conference on Lasers and Electro-Optics and European Quantum Electronics Conference*. Optical Society of America, 2017. URL: http://www.osapublishing.org/abstract.cfm?URI=EQEC-2017-EF_2_1.

[Mar+14] M. Marconi et al. "How Lasing Localized Structures Evolve out of Passive Mode Locking". In: *Phys. Rev. Lett.* 112 (22 June 2014), p. 223901. DOI: 10.1103/PhysRevLett.112.223901. URL: https://link.aps.org/doi/10.1103/PhysRevLett.112.223901.

[SS13] Kestutis Staliunas and Víctor Sánchez-Morcillo. *Transverse Patterns in Nonlinear Optical Resonators*. June 2013.

[Str94] Steven H. Strogatz. *Nonlinear Dynamics and Chaos*. 1994.

[Thi17] Uwe Thiele. *Numerical Continuation - A step by step introduction Prelude to the Münsteranian Torturials*. http://www.uni-muenster.de/CeNoS/Lehre/Tutorials/continuation.html. 2017.

[Vla+97] A G Vladimirov et al. "Bifurcation analysis of laser autosolitons". In: *Quantum Electronics* 27.11 (1997), p. 949. URL: http://stacks.iop.org/1063-7818/27/i=11/a=A04.

[YCS08] A. V. Yulin, A. R. Champneys, and D. V. Skryabin. "Discrete cavity solitons due to saturable nonlinearity". In: *Phys. Rev. A* 78 (1 July 2008), p. 011804. DOI: 10.1103/PhysRevA.78.011804. URL: https://link.aps.org/doi/10.1103/PhysRevA.78.011804.

Eidesstattliche Erklärung

Hiermit versichere ich, Thomas Seidel, dass die vorliegende Arbeit mit dem Titel *Dynamics of discrete light bullets in passively mode-locked semiconductor lasers* selbstständig verfasst worden ist, dass keine anderen Quellen und Hilfsmittel als die angegebenen benutzt worden sind und dass die Stellen der Arbeit, die anderen Werken – auch elektronischen Medien – dem Wortlaut oder Sinn nach entnommenen wurden, auf jeden Fall unter Angabe der Quelle als Entlehnung kenntlich gemacht worden sind.

Ich erkläre mich mit einem Abgleich der Arbeit mit anderen Texten zwecks Auffindung von Übereinstimmungen sowie mit einer zu diesem Zweck vorzunehmenden Speicherung der Arbeit in eine Datenbank einverstanden.

Münster, den 10. September 2018

Thomas Seidel